Quantum-critical properties of long-range Heisenberg ladders with quantum Monte Carlo simulations

Masters Thesis in Physics

Presented by

Florian Simon

24.05.2024

Chair for Theoretical Physics V
Friedrich-Alexander-Universität Erlangen-Nürnberg
Supervisor: Prof. Dr. Kai Phillip Schmidt

Abstract

We investigate the quantum criticality between the rung-singlet phase and the SU(2)-symmetry broken Néel phase of the spin-$\frac{1}{2}$ Heisenberg model with unfrustrated algebraically decaying long-range ferromagnetic and antiferromagnetic Heisenberg interections on two one dimensional two leg quantum spin ladders. For this, the quantum Monte Carlo stochastic series expansion method is implemented. The convergence to effective zero-temperature is ensured by gradually cooling down the system. The critical points and exponents β, γ and ν are extracted using finite-size scaling methods like data collapse and Binder ratios. In the quantum Monte Carlo scheme, systems of up to 1024 spins are simulated and the critical behavior across the whole phase diagram is examined. The results of other works on these models are confirmed, as well as connections to the antiferromagnetic long-range Heisenberg spin-$\frac{1}{2}$ chain are drawn. The quantum Monte Carlo data is set in relation to spin wave calculations from other works. Upper critical decay exponents σ, above which no long-range order exists, are calculated for both models. The quantum critical exponents are compared to pCUT data from other works and functional renormalization group (FRG) calculations. There we find that our data is in good agreement with other works and FRG predictions. The problems and limitations we faced are discussed in detail as well as opportunities for further investigations and open questions are presented.

Contents

1 Introduction

Over the years, Heisenberg spin-$\frac{1}{2}$ ladder models have been a subject of great interest in condensed matter physics. Heisenberg spin chains with nearest-neighbor interactions are well understood since the 1930s [3], coupling more and more of such spin chains together allows to understand the physics of planes. In between Heisenberg spin ladders are located, the introduction of a perpendicular binding allows the tuning of parameters and quantum phase transitions which will be shown later in this thesis. Antiferromagnetic Heisenberg spin-$\frac{1}{2}$ next neighbor ladders are known to have a real world application in the form of certain types of cuprates [16] and other copper compounds [26]. It is also known, that antiferromagnetic 1d-Heisenberg models like ladders do not exhibit long-range order with only nearest-neighbor interactions, which will be adressed later.

This becomes possible through the introduction of long-range interactions with algebraic decay, which makes systems including such interactions interesting. Long-range interactions are not common in the most solid state applications though, as most often only next neighbor interactions account. But such long-range interactions can emerge in certain constellations, n particular in most quantum-optical platforms [7]. A recent review [7] of the current state of the field shows, that long-range spin interactions with tunable decay exponents can be realized in experiments by laser-cooled ions in radio-frequency traps. Such systems are discussed for utilization in quantum computing and quantum simulation [24, 31]. Other experimantal realizations of long-range systems are cold atomic gases in cavities as well as dipolar and Rydberg systems [7].

Whereas unfrustrated long-range Ising models are widely investigated in the past [22, 11, 12], less is known about frustrated long-range Ising models [21].

The antiferromagnetic long-range Heisenberg spin-$\frac{1}{2}$ ladders discussed in this thesis were examined before in other works [1, 42] and related systems such as the spin-$\frac{1}{2}$ long-range Heisenberg chain have also been the subject of investigation [25]. Where in Ref. [42] the nature of the phase transition was not clear, [1] expanded on that by painting a bigger picture across the phase diagram, incorporating two types of long-range ladder models.

This thesis will further expand on those models. The SSE quantum Monte Carlo method will be used to map out the phase transition over the whole phase diagram to complete the picture illustrated in Ref. [1]. The magnetization and susceptibility emerging in the ladder systems will be calculated and the quantum critical exponents extracted from the behavior of those observables at the critical point. This builds on the previous work on these systems [1], with a different method it is expected to clarify the continously varying behavior of the exponents there.

This thesis is structured as follwos: In section 2 the basic concept of quantum phase transitions and the quantities which characterize them will be discussed shortly. In section 3 the models, their expected behavior and theoretical expectations will be introduced. In section 4 the methods used in this thesis will be explained in detail and how the quantum critical points and exponents are extracted from the raw data will be shown. In section 5 the results obtained in this way will be shown and discussed in the context of other works and theoretical calculations to get the full picture of these models.

2 Quantum Phase Transitions

To outline the concept of quantum phase transitions investigated in this thesis, at first we will give a short introduction to classical phase transitions. We will then turn to quantum phase transitions to introduce the properties in which we are interested.

Phase transitions are often categorized into two types. There are first-order phase transitions and those of higher order (continuous phase transitions) [8]. In this thesis especially phase transitions of the second order are investigated. A classical first-order phase transition is characterized by the exchange of heat which causes discontinuity in quantities like the entropy or the volume [8]. These phase transitions are called first order, because the discontinuities occur in the first derivatives of the Gibbs-potential [8].

2.1 Continuous phase transitions

Continuous phase transitions on the other hand are often characterized by a symmetry breaking [8]. In the case of the antiferromagnetic phase transitions, this means that the two phases obey different symmetry groups, one of which is a sub group of the other. So one phase has a higher symmetry than the other which allows the introduction of an order parameter which characterizes the phase transition [8, 34]. In contrast to first-order phase transitions, the entropy is continuous and singularities in the second derivatives of the free energy arise [8].

Landau theory allows a description of phase transitions with symmetry breaking [8]. Here the free energy is a functional of the order parameter, which is zero in the high-symmetry phase and finite in the lower symmetry phase (symmetry-broken phase) [8]. A typical Landau ansatz for magnetic systems is given by an expansion of the free energy in the magnetization m. Mainly second and fourth powers of m are incorporated, but fluctuations in m can also be addressed by incorporating derivatives of m [8, 34].

$$F[m] = rm^2 - um^4 \tag{1}$$

Equation 1 describes a simple Landau ansatz where the phase transition is driven by a parameter r. The phase transition occurs for $r = 0$, as the minima of the free engery functional shift from two possible minima to just one [8]. For a thermal phase transition one would take this parameter to be the reduced temperature: [20]

$$r = \frac{T - T_c}{T_c}. \tag{2}$$

Following [34], a quantum phase transition is a phase transition in the ground-state of a quantum system at temperature $T = 0$. The phase transition is driven by quantum fluctuations, in contrast to thermal phase transitions driven by temperature fluctuations. The transition is induced by a control parameter g in the Hamiltonian. So the Hamiltonian is a smooth function of this parameter:

$$\mathcal{H} = \mathcal{H}(g). \tag{3}$$

A quantum phase transition at g_c causes a nonanalyticity in the ground-state energy, due to an excited energy level crossing into the ground-state level at g_c. This is only the case in the thermodynamic limit on infinite systems, on finite systems this level crossing is avoided but gets sharper with larger system sizes [34].

The continuous quantum phase transitions are (like in the classical case) characterized by a symmetry breaking and discontinuities in second derivatives of the free energy (for example the correlation length and susceptibility) [34].

2.2 Critical exponents

In Landau theory the behavior of certain quantities of interest in the vicinity of g_c are given by a power law [34]. The exponents of these quantities are called critical exponents. An approach to determine them is renormalization group theory [34]. The free energy functional F is transformed by a rescaling of space-time and under the assumption that F must be invariant, rescaling of other quantities involved in F, such as the magnetization, susceptiblity, control parameter and others can be determined [34]. One finds, that certain quantities are irrelevant, which means their scaling exponent is negative. Under multiple rescalings, these quantities vanish. One expects the other quantities at the critical point to be the limit of infinite repeated rescalings [34]. So these irrelevant quantities do not affect the critical point behavior as they vanish there [28]. This is only true below the upper critical dimension [28], further discussion on this will be provided in 4.5.2.

Typically, the microscopic properties of a system are irrelevant close to a (quantum) critical point, such that one can cluster different systems in a class, in which all exhibit the same critical behavior [34]. The critcal behavior is universal in this universality class and is only determined by macroscopic properties of the system, typically the control parameter, dimensionality, symmetry and others. [34]

The critical exponents investigated in this thesis are given in table 1.

Exponent	power law	quantity	definition
β	$M \propto (g-g_c)^{\beta}$	order parameter	$m = \frac{\partial f}{\partial H}\|_{H=0}$
γ	$\chi \propto (g-g_c)^{-\gamma}$	order parameter susceptibility	$\chi = \frac{\partial^2 f}{\partial H^2}\|_{H=0}$
ν	$\xi^{-1} \propto (g-g_c)^{\nu}$	correlation length ξ	
z	$\xi_\tau \propto \xi^z$	correlation length in imaginary time	
	$\Delta \propto (g-g_c)^{\nu z}$	energy gap Δ	

Table 1: Critical exponents and the quantities they describe [34, 20].

2.3 Scaling relations

As described by [34] and [20] with field theory and the renormalization group formalism, relations between the critical exponents can be derived:

$$\gamma = \beta(\delta - 1) \tag{4}$$

$$2 = \alpha + 2\beta + \gamma \tag{5}$$

$$\gamma = (2-\eta)\nu \tag{6}$$

$$\alpha = 2 - \nu(d+z) \tag{7}$$

with d the spatial dimension of the system. These so called scaling relations will later be used to determine a full set of exponents, as only γ, β and ν will be measured in the QMC simulations.

3 Models

The models discussed in this thesis are antiferromagnetic Heisenberg spin-$\frac{1}{2}$ ladder models. Among others Ising models and Heisenberg models are used to describe the characteristics and phase transitions of magnetic systems. In contrast to the Ising spin, which can only take on two values (± 1), the Heisenberg spin is a three dimensional vector $\overrightarrow{S} = (S_x, S_y, S_z)$, described by the angular momentum algebra [34]. So depenendent on the total spin (which is $S = \frac{1}{2}$ here), the spin component in preferred direction (without loss of generality S_z) can take on more values in between $+S$ and $-S$. Another important difference is, that Heisenberg spin models are invariant under spatial rotation [34].

In the models described in the following sections, Heisenberg $\frac{1}{2}$-spins are placed pairwise to form a ladder structure. The bonds are chosen in such a way that each spin interacts with its neigbors antiferromagnetically, which means, that an anti-alignment of the spins is preferred energetically. Dependent on the structure of the underlying lattice, such interactions could lead to frustration. That would mean that conflicting bonds act on a single spin, so it is not directly clear which alignment is more energetically preferrable. The bonds in the following models are chosen in such a way that this will not happen, they are unfrustrated.
To understand the behavior of the long-range Heisenberg ladders, which are the main focus of this thesis, first the ladder model with only nearest-neighbor interactions is described. After that two different systems with long-range interactions are introduced and the underlying theoretical calculations are explored.

3.1 Antiferromagnetic Heisenberg ladder with nearest-neighbor interactions

Although not simulated in this thesis, it is useful to take a look at the antiferromagnetic nearest-neighbor Heisenberg ladder model, to understand its long-range counterparts better. The Hamiltonian is given by

$$\mathcal{H}_{\mathrm{NN}} = J_{\perp} \sum_{i} \overrightarrow{S}_{i,1} \cdot \overrightarrow{S}_{i,2} + J_{\parallel} \sum_{i} \sum_{n=1}^{2} \overrightarrow{S}_{i,n} \cdot \overrightarrow{S}_{i+1,n} \ , \ J_{\perp}, J_{\parallel} \geq 0. \tag{8}$$

with summation over rungs i. The sign of the bonds is chosen in such a way that over all the model is antiferromagnetic and unfrustrated.
In the limit of $J_{\parallel} = 0$ (strong coupling), the ground state takes the form of a product state over rung singlets $|s\rangle = \frac{|\uparrow\downarrow\rangle - |\downarrow\uparrow\rangle}{\sqrt{2}}$ [16]. With the corresponding rung triplet as the elementry excitations [16]

$$|t_x\rangle = -\frac{|\uparrow\uparrow\rangle - |\downarrow\downarrow\rangle}{\sqrt{2}}, \ |t_y\rangle = \frac{|\uparrow\uparrow\rangle + |\downarrow\downarrow\rangle}{\sqrt{2}} \text{ and } |t_z\rangle = \frac{|\uparrow\downarrow\rangle + |\downarrow\uparrow\rangle}{\sqrt{2}}. \tag{9}$$

From this limit the rung-singlet state evolves smoothly for $J_\parallel/J_\perp < \infty$ with a gapped excitation spectrum [40]. The excitations can be understood as triplons (triplet quasi-particles) [38]. For $J_\parallel = \infty$ the two spin-$\frac{1}{2}$ chains decouple and the one-triplon gap closes [16]. Since no long-range order is allowed to exist [30, 18], as the gap closes, a spin liquid ground state with algebraically decaying correlations is formed [5].

3.2 Ladder with long-range interactions along the legs

The model is given by the following Hamiltonian:

$$\mathcal{H}_\parallel = J_\perp \sum_i \overrightarrow{S}_{i,1} \cdot \overrightarrow{S}_{i,2} - \sum_{i,\delta>0} \sum_{n=1}^{2} J_\parallel(\delta) \overrightarrow{S}_{i,n} \cdot \overrightarrow{S}_{i+\delta,n} \tag{10}$$

with $S = \frac{1}{2}$, where the first index denotes the site and the second index denotes the leg of the ladder. The interaction strength along the legs is given by:

$$J_\parallel(\delta) = \lambda \frac{(-1)^\delta}{|\delta|^{1+\sigma}}. \tag{11}$$

The model realizes long-range interactions along the legs in addition to antiferromagnetic ineractions between the legs. The signs of the bonds are chosen in such way, that the system is unfrustrated.

The Hamiltonian is invariant under spin rotations and therefore has a continous $SU(2)$-symmetry. Without long-range interactions, no phase transition to an antiferromagnetically ordered state is possible. Due to the Mermin-Wagner-Hohenberg theorem no long-range antiferromagnetic order can exist in one- or two-dimensional systems at $T > 0$ [30, 18] and in one dimensional systems at $T = 0$ [33]. This rule is circumvented by the introduction of long-range interactions and a long-range antiferromagnetic order can form [17] in this one-dimensional model.

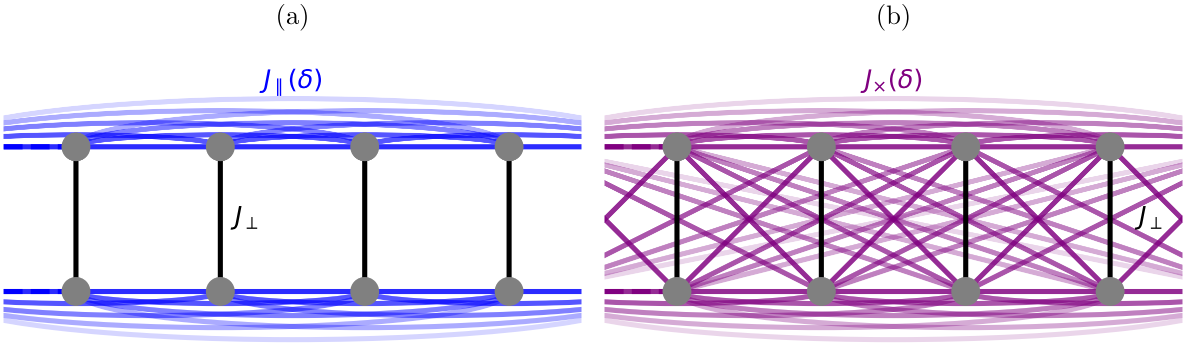

Figure 1: The two models examined in this thesis. (a) Heisenberg ladder with long-range interactions only along the legs. (b) Heisenberg ladder with long-range interactions in and between the legs.

Here σ quantifies the algebraic decay of the long-range interactions. For $\lambda = \infty$ the ladder decouples into two Heisenberg chains. The limiting case for $\sigma = \infty$ ($\lambda = 0$) is a product state of decoupled antiferromagnetic dimers on the rungs. This is true for both the parallel and cross leg interaction

models, as the perpendicular interactions are always left constant.
This limiting case also forms the aforementioned rung singlet product state. The rung singlet phase is characterized by a continuous spin rotational symmetry and an energy gap between the rung singlet and its excitations.
For strong long-range interactions (σ small), the continuous rotational symmetry of the system is broken and the aforementioned long-range antiferromagnetic (Néel) order is realized. The Néel order is defined by a finite sublattice magnetization in two different directions on the two different sublattices (shown in Fig. 2). It is gapless, and its excitations are spin waves (Nambu Goldstone modes) [32, 14, 15].

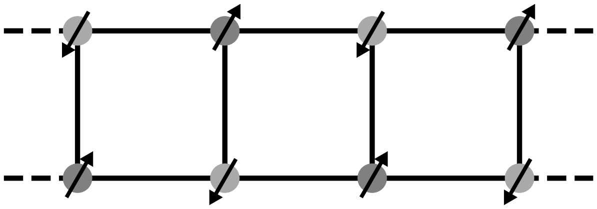

Figure 2: Heisenberg ladder in a Néel state with finite sub lattice magnetization, one sublattice is colored in dark gray and the other in lightgray, the spins are orientated in an antiferromagnetic order.

An order parameter to quantify the sublattice magnetization is the staggered magnetization. As the observable should be zero in the symmetric phase and finite in the symmetry broken phase, one defines it like the normal magnetization, but with a phase factor that takes into account the antiferromagnetic ordering of the two sublattices. As the expectation value of the magnetization vanishes in finite systems [4], the z-componnet of the squared staggered magnetization is defined as

$$m_z^2 = \left(\frac{1}{L} \sum_{l \in \{0,1\}} \sum_{r=0}^{L/2-1} S^z_{lL/2+r} e^{i\pi(l+r)} \right)^2 \tag{12}$$

with summation over the legs l and rungs r of the ladder. In the rung-singlet phase this squared magnetization is zero, whereas deep in the Néel phase, it takes on its maximal value. There, the magnetization per site takes on a value of $\frac{1}{12} = \frac{1}{4}\frac{1}{3}$ with $\frac{1}{4}$ the maxmial value of the squared magnetization operator and $\frac{1}{3}$ because only one of three components of the magnetization vector is considered.

3.3 Ladder with cross leg interactions

In addition to the parallel ladder, here long-range interactions across the legs are also included in the Hamiltonian, again chosen in such a way that the system stays unfrustrated.
The model is given by the following Hamiltonian:

$$\mathcal{H}_\times = J_\perp \sum_i \overrightarrow{S}_{i,1} \cdot \overrightarrow{S}_{i,2} - \sum_{i,\delta>0} \sum_{n=1}^{2} J_\parallel(\delta) \overrightarrow{S}_{i,n} \cdot \overrightarrow{S}_{i+\delta,n} - \sum_{i,\delta>0} J_\times(\delta) \overrightarrow{S}_{i,1} \cdot \overrightarrow{S}_{i+\delta,2}. \tag{13}$$

The interaction strength for the cross leg interactions is given by:

$$J_{\times}(\delta) = \lambda \frac{(-1)^{\delta+1}}{(\delta^2+1)^{\frac{1+\sigma}{2}}}. \tag{14}$$

The limiting case $\lambda = 0$ here also is the rung-singlet phase. For small σ as in the parallel ladder, a Néel phase is realized. A difference is, that for $\lambda = \infty$ the two Heisenberg chains will not decouple, instead a diagonal spin ladder forms. Decoupling is only expected for $\lambda = \infty$ and $\sigma = \infty$, since the the cross leg inetractions disappear and the limiting case of the parallel ladder at $\lambda = \infty$ is recovered [1].

3.4 Field theory calculations

The low energy properties of unfrustrated long-range Heisenberg ladder models can be mapped to the quantum rotor model [34]. One can describe the long-range ordered Néel phase by such quantum rotor calculations [1]. The discrete magnetization of the system can be described by a three component field $\overrightarrow{\phi}$ via coarse graining ansatz [34]:

$$\overrightarrow{\phi}(x,\tau) \propto \sum_{i \in \mathcal{N}(x)} \overrightarrow{S}_i \tag{15}$$

where $\mathcal{N}(x)$ is a coarse-graining neighborhood of x. For the long-range quantum rotor model one can write the mean field partition function as an integral over all values of $\overrightarrow{\phi}$.

$$\mathcal{Z} = \int D\overrightarrow{\phi}(x,\tau) e^{-S_\phi} \tag{16}$$

The action S_ϕ can be written as an extension of the free energy of Landau theory as an integral over space and imaginary time:

$$S_\phi = \int dx \int d\tau \left[\left(\partial_\tau \overrightarrow{\phi}(x,\tau)\right)^2 + \left(\partial_x \overrightarrow{\phi}(x,\tau)\right)^2 + r\,\overrightarrow{\phi}(x,\tau)^2 + \int dy \frac{\overrightarrow{\phi}(x,\tau)\phi(y,\tau)}{|x-y|^{1+\sigma}} \right] + u \int dx \int d\tau\, \overrightarrow{\phi}(x,\tau)^4. \tag{17}$$

This can be Fourier transformed to obtain [9]:

$$S_{\tilde{\phi}} = \frac{1}{2} \int dq \int d\omega \left[g\omega^2 + r + aq^\sigma + bq^2 \right] \overrightarrow{\phi}(q,i\omega)\,\overrightarrow{\phi}(-q,-i\omega) + u \int dx \int d\tau \left(\overrightarrow{\phi}(x,\tau) \right)^4. \tag{18}$$

One now rescales the space (momentum q) by a factor k to the power of spatial dimension, which is 1 in this case. The imaginary time (frequency ω) is scaled by k^z, where z is the space-time-anisotropy which can be identified by the critical exponent z. r, u and ϕ are also rescaled by k to powers which are to be determined:

$$\omega = k^{-z}\omega', \quad q = k^{-1}q', \quad r = k^{[r]}r', \quad u = k^{[u]}u', \quad \overrightarrow{\phi} = k^{[\phi]}\overrightarrow{\phi}'. \tag{19}$$

One is interested in the behavior at small q because this corresponds to the long-range behavior. Therefore the leading term in q is aq^σ for $\sigma < 2$ and bq^2 for $\sigma \geq 2$. The case where long-range

interactions dominate is for $\sigma < 2$, so bq^2 can be dropped.
For the action one obtains:

$$\begin{aligned} S'_{\tilde{\phi}} = \frac{1}{2}\int dq \int d\omega \left[k^{-d-z+2z+2[\phi]} g'\omega'^2 + k^{-d-z+[r]+2[\phi]} r' + k^{-d-z+d\sigma+2[\phi]} a q'^{\sigma}\right] |\overrightarrow{\tilde{\phi}}(q,\omega)|^2 + \\ \int dx \int d\tau k^{-1-z+[u]+4[\phi]} |\overrightarrow{\tilde{\phi}}(q,\omega)|^4 . \end{aligned} \tag{20}$$

One demands, that the action is invariant under the rescaling $S_\phi = S'_\phi$, so the powers of k have to vanish, which leads to the following system of equations:

$$\begin{aligned} &-1-z+2z+2[\phi]=0 \\ &-1-z+[r]+2[\phi]=0 \\ &-1-z+\sigma+2[\phi]=0 \\ &-1-z+[u]+4[\phi]=0. \end{aligned} \tag{21}$$

Solving these equation yields the following exponents:

$$\begin{aligned} &z=\frac{\sigma}{2} \\ &[r]=2z=\sigma \\ &[\phi]=\frac{1-z}{2}=\frac{1}{2}-\frac{\sigma}{4} \\ &[u]=-1+3z=-1+\frac{3\sigma}{2}. \end{aligned} \tag{22}$$

These exponents can be identified with the quantum critical exponents z, ν and β [34]. The exponent $[u]$ defines the upper critical dimension d_{uc}, below which one expects mean field behavior [34]. Below the upper critical dimension u is irrelevant, at the upper critcal dimension $[u] = 0$. Therefore

$$d_{uc} = \frac{3\sigma}{2}. \tag{23}$$

And one expects long-range mean field behavior for

$$d < d_{uc} \Leftrightarrow \sigma < \frac{2}{3}. \tag{24}$$

The long-range mean field critical exponents are then:

$$\begin{aligned} &z=\frac{\sigma}{2} \\ &\nu=\frac{1}{[r]}=\frac{1}{\sigma} \\ &\beta=\frac{1}{2} \\ &\gamma=1 \end{aligned} \tag{25}$$

where the value for γ is taken from Ref. [9] and the value for β is calculated from Ref. [9] via the scaling relations.

3.5 Spin wave calculations

The Néel phase and its excitations can be understood with linear spin wave theory [37]. There, fluctuations in the antiferromagnetic order are mapped to bosons [37]. spin wave theory is exact for $S \to \infty$, for finite S it is an approximation, which is improved in the form of an expansion in $1/S$ [37]. Following [1], the results for such a spin wave approximation can be derived.
The ansatz is a mapping of the spin operators to bosonic creation and annihilation operators using the Holstein-Primakoff transformation up to linear order [1, 19].
The spin wave dispersion for the $\mathcal{H}_{\parallel}$-model is found to be

$$\omega_{\pm}^{\mathcal{H}_{\parallel}^{SW}}(k) = \sqrt{(B - f(k))^2 - (g(k) \pm 1)^2}. \tag{26}$$

with λ and σ dependent functions B, $f(k)$, $g(k)$. From that one can calculate the magnetization in the Néel state [1]:

$$m = S - \Delta m = S - \frac{1}{\pi} \int_{-\pi/2}^{\pi/2} dk \left[\frac{1}{2} \left(\frac{B - f(k)}{\omega_+(k)} + \frac{B - f(k)}{\omega_-(k)} \right) - 1 \right]. \tag{27}$$

For the $\mathcal{H}_{\times}$-model one finds [1]

$$\omega_{\pm}^{\mathcal{H}_{\times}^{SW}}(k) = \sqrt{\left[B_{\times} - (f(k) \pm w(k))\right]^2 - (g(k) \pm v(k))^2} \tag{28}$$

and

$$m = S - \Delta m = S - \frac{1}{\pi} \int_{-\pi/2}^{\pi/2} dk \left[\frac{1}{2} \left(\frac{B_{\times} - f(k) - w(k)}{\omega_+(k)} + \frac{B_{\times} - f(k) + w(k)}{\omega_-(k)} \right) - 1 \right] \tag{29}$$

with λ and σ dependent functions $B_{\times}$, $w(k)$ and $v(k)$. From this, one can approximate the critical point in λ and σ by the consistency condition $\Delta m < S$ [1, 43, 25].

4 Methods

In the previous section, the models as well as their theoretically approximated behavior was presented. From other works [1] it is known, that the mean field predictions should hold in their respective range. It is a goal of this thesis to confirm this finding, as well as further investigate the regime, where the mean field predictions do not hold anymore. In this regime, [1] suggests continuosly varying critcal exponents, but the findings are not accurate for larger σ, because the method used there breaks down for larger σ. This manifests in unphysical diverging exponents, and the methods used in this thesis can give a more reliable answer for the behavior there. There are also open questions regarding an upper critical σ and theoretical predictions made through functional renormalization group (FRG) [6]. These points will be addressed in the section 5. The methods used to derive the results discussed there will be introduced in the following sections.

4.1 Monte Carlo Integration

The results in this thesis are obtained through Monte Carlo methods, the basics of which will be discussed in the following section. These explanations mainly follow [23]

Monte Carlo methods can be used to approximate integrals that otherwise would be difficult to calculate. This is done by sampling many random configurations and taking the mean. Here, this will be used to calculate the expectation values of the relevant observables to calculate the quantum phase diagram of long-range Heisenberg ladders.

The observables to be calculated are of the form

$$\langle O \rangle = \int_C O(x)P(x)dx \tag{30}$$

where C is the configuration space, and P is the underlying probability distribution of the states that are to be sampled. So $P(x)$ denotes the probability that the system will be in the state $x \in C$. The approximation drawing N random samples from C will then be the drawn sample states weighted by P divided by the sum of weights.

$$\langle O \rangle \approx \bar{O} = \frac{\sum_{i=1}^{N} P(x_i)O(x_i)}{\sum_{i=1}^{N} P(x_i)} \tag{31}$$

4.2 Markov chain Monte Carlo

Direct sampling is not as relevant for this thesis as Markov chain sampling, which is used for the SSE method described in the next section. There the points are not directly drawn from a given distribution, but determined by calculating random walks starting from an initial point. The points in such a random walk are the so called “Markov chain”.

The Markov chain fulfills the Markov property, which is, that the next state in the chain only depends on the current state and not on the other states that came before it. So in every step of the random walk, the new point is determined only by a random jump from the current point. This probability to go from one state to the next must fullfill the detailed balance condition. This ensures, that the Markov chain really samples from the underlying distribution $P(x)$ (for stationary distributions, at least global balance must be fulfilled) [23]. The detailed balance condition is given by

$$P(x)p(x \to y) = P(y)p(y \to x) \tag{32}$$

where $p(x \to y)$ is the probability to go from state x to state y. A popular algorithm that fulfills the detailed balance condition is the Metropolis-algorithm. This is achieved by choosing the acceptance probability to be

$$p(a \to b) = \min\left(1, \frac{P(b)}{P(a)}\right). \tag{33}$$

One can easily check, that with this definition the detailed balance is fulfilled. An extension to this is the Metropolis-Hastings-algorithm. The probability for a move from a to b is decomposed into an proposal probability $\mathcal{A}$ and an acceptance probability $\mathcal{P}$ [23]

$$\mathcal{P}(a \to b) = \mathcal{A}(a \to b) \cdot p(a \to b). \tag{34}$$

The acceptance probability is then generalized to [23]

$$p(a \to b) = \min\left(1, \frac{P(b)}{\mathcal{A}(a \to b)} \frac{\mathcal{A}(b \to a)}{P(a)}\right). \tag{35}$$

4.3 Transition to quantum Monte Carlo

When sampling classical physical systems like thermodynamic problems, the underlying probability distribution, which should be sampled, will be given by the partition function. As known from thermodynamics [2] the partition function holds the probabilities that the system realizes a microstate x:

$$p(x) = \frac{e^{-\beta E(x)}}{Z}; \quad Z = \sum_x e^{-\beta E(x)} \tag{36}$$

This is not the case for quantum systems where the partition function is given by the trace [36]

$$Z = \operatorname{tr}\left(e^{-\beta H}\right) = \sum_{\{|\alpha\rangle\}} \langle\alpha| e^{-\beta H} |\alpha\rangle. \tag{37}$$

Without knowing the eigenstates and eigenenergies of the system in advance, this partition function cannot be decomposed like in a classical system [35]. Therefore quantum Monte Carlo methods like SSE attempt to rewrite the Hamiltonian and the partition function so it decomposes into a sum of probability weights similar to the classical case [35]

$$Z = \sum_{x \in C} w(x) \tag{38}$$

with a configuration space not necessarily given only by quantum states. This decomposition for SSE quantum Monte Carlo is investigated further in the next section.

Another problem with quantum systems for QMC approaches, that should be briefly adressed is the sign problem [29]. Although it does not occur in the systems discussed in this thesis, it is an infamous problem in quantum Monte Carlo. The sign problem arises due to the expressions $\langle\alpha|\cdot|\alpha\rangle$ not necessarily giving a non negative value, and therefore the weights $w(x)$ are not always being positive. This is especially the case with fermionic statistics and in frustrated systems. Nevertheless it is possible to sample these systems with quantum Monte Carlo, but one has to take the absolute values of the weights $|w(x)|$. The observables are then given by [41]

$$\langle O\rangle_w = \frac{\langle O \ \mathrm{sgn}(w)\rangle_{|w|}}{\langle \mathrm{sgn}(w)\rangle_{|w|}}. \tag{39}$$

The problem with this is, that the average sign $\langle \mathrm{sgn}(w)\rangle_{|w|}$ vanishes at small temperatures and large system sizes [41]. So for simulations at low temperatures and on large systems this becomes a problem, as the relative error on the sign rises exponentially and propagates to all observables [41].

4.4 Stochastic Series Expansion

The Stochastic Series Expansion (SSE) Monte Carlo method was introduced by A. Sandvik [35], our follwing descriptions will therefore closely follow Sandviks works [35, 37, 39].

4.4.1 Representation of the Partition Function

The Hamiltonian is decomposed into a finite set of operators, the decomposition of the Hamiltonian and the roles of the indices a and b will become clear, when we discuss the implementation of the antiferromagnetic long-range Heisenberg model in section 4.4.2.

$$\mathcal{H} = -\sum_{a,b} H_{a,b} \tag{40}$$

The partition function is given by:

$$Z = \mathrm{tr}\left(e^{-\beta\mathcal{H}}\right) \tag{41}$$

which can be expanded with the Taylor series:

$$Z = \sum_{n=0}^{\infty} \frac{(-\beta)^n}{n!} \mathrm{tr}\left(\mathcal{H}^n\right). \tag{42}$$

The trace is evaluated in a chosen computational basis $|\alpha\rangle$ and with the decomposition (40) this yields

$$\begin{aligned} Z &= \sum_{n=0}^{\infty} \frac{(-\beta)^n}{n!} \sum_{\{|\alpha\rangle\}} \langle\alpha| (-\sum_{a,b} H_{a,b})^n |\alpha\rangle \\ &= \sum_{n=0}^{\infty} \sum_{\{|\alpha\rangle\}} \frac{\beta^n}{n!} \langle\alpha| (\sum_{a,b} H_{a,b})^n |\alpha\rangle . \end{aligned} \tag{43}$$

The powers are further expanded by evaluating all possible products of operators and introducing a sequence of the corresponding indices $S_n = [a_0, b_0], ..., [a_{n-1}, b_{n-1}]$

$$\left(\sum_{a,b} H_{a,b}\right)^n = \sum_{\{S_n\}} \prod_{p=0}^{n-1} H_{a_p,b_p}. \tag{44}$$

Inserting this into the expansion finally leads to

$$Z = \sum_{n=0}^{\infty} \sum_{\{S_n\}} \sum_{\{|\alpha\rangle\}} \frac{\beta^n}{n!} \langle\alpha| \prod_{p=0}^{n-1} H_{a_p,b_p} |\alpha\rangle\,, \tag{45}$$

which represents the sum of weights $w(S_n, \alpha)$ for the Monte Carlo scheme over the configuration space

$$C = \{|\alpha\rangle\} \times \cup_{n=0}^{\infty} \{S_n\}. \tag{46}$$

Every configuration can be uniquely described by a state $|\alpha\rangle$ and the sequence S_n, $|\alpha\rangle$ is propagated by every operator in the sequence, yielding a series of propagated operators

$$|\alpha(p)\rangle = \prod_{i=0}^{p-1} H_{a_i,b_i} |\alpha\rangle \tag{47}$$

with $|\alpha(0)\rangle = |\alpha\rangle$. The propagation direction can be seen as proportional to the imaginary time [37]. This leads to the periodic boundary condition in imaginary time $|\alpha(0)\rangle = |\alpha(n)\rangle$. This is because the weights of all configurations which do not fulfil this condition vanish due to the trace.

Because of the finite nature of numeric computations, the Taylor expansion (42) must be truncated at an index $n = \mathcal{L}$. This means a maximum length $\mathcal{L}$ for all possible sequences $S_{\mathcal{L}}$. To simplify the calculations, one assumes this finite length for all sequences. The sequences shorter than $\mathcal{L}$ are then padded out with identity operators, noted as $H_{0,0} = 1$.
One has $\binom{\mathcal{L}}{\mathcal{L}-n(S_{\mathcal{L}})}$ possibilities to insert those identity operators, which costs a factor in the sum of weights. The sum over n is resolved by this and n goes to $n(S_{\mathcal{L}})$, which now denotes the number of operators in the sequence, that are not identity.

$$Z = \sum_{\{S_{\mathcal{L}}\}} \sum_{\{|\alpha\rangle\}} \frac{\beta^{n(S_{\mathcal{L}})}(\mathcal{L} - n(S_{\mathcal{L}}))!}{\mathcal{L}!} \langle\alpha| \prod_{p=0}^{\mathcal{L}-1} H_{a_p,b_p} |\alpha\rangle \tag{48}$$

This does not mean, the sequence length is fixed during the Monte Carlo run. The sequence length is rather adjusted after every Monte Carlo step according to the filling of the sequence with non trivial operators. This filling should not exceed 0.75 [37].

4.4.2 Operators and Updates for Heisenberg models

As a reminder, the studied models are given by:

$$\begin{aligned}
&\mathcal{H} = J_\perp \sum_i \overrightarrow{S}_{i,1} \cdot \overrightarrow{S}_{i,2} - \sum_{i,\delta>0} \sum_{n=1}^{2} J_\parallel(\delta) \overrightarrow{S}_{i,n} \cdot \overrightarrow{S}_{i+\delta,n} - \sum_{i,\delta>0} J_\times(\delta) \overrightarrow{S}_{i,1} \cdot \overrightarrow{S}_{i+\delta,2} \\
&\mathcal{H}_\parallel = \mathcal{H}|_{J_\times=0} \\
&\mathcal{H}_\times = \mathcal{H}|_{J_\parallel=J_\times} \\
&J_\parallel(\delta) = \lambda \frac{-1^\delta}{|\delta|^{1+\sigma}},\ J_\times(\delta) = \lambda \frac{(-1)^{\delta+1}}{(\delta^2+1)^{\frac{1+\sigma}{2}}}
\end{aligned} \tag{49}$$

The scalar product of the Heisenberg interaction can be written as:

$$\overrightarrow{S}_{i,k} \cdot \overrightarrow{S}_{j,l} = S^x_{i,k} S^x_{j,l} + S^y_{i,k} S^y_{j,l} + S^z_{i,k} S^z_{j,l}. \tag{50}$$

As the computational basis the S^z basis is chosen $\{|\alpha\rangle\} = \{|S^z_1, ..., S^z_{2L}\rangle\}$ with L the number of dimers of the ladder. In this basis the $S^z_i S^z_j$ part of the interaction is diagonal and the $S^x_i S^x_j + S^y_i S^y_j$ parts off-diagonal and perform spin flips. With this, the model can be decomposed into the following operators:

$$\begin{aligned}
H_{0,0} &= 1 \\
H^d_{i,j} &= J_{ij} S^z_i S^z_j \\
H^{od}_{i,j} &= J_{ij}\left(S^x_i S^x_j + S^y_i S^y_j\right) = \frac{J_{ij}}{2}\left(S^+_i S^-_j + S^-_i S^+_j\right).
\end{aligned} \tag{51}$$

4.4.3 Diagonal update

Inititally, the sequence starts with only trivial identity operators. In the diagonal update, these trivial operators are swapped for diagonal $S^z S^z$ interaction operators. As well as diagonal operators swapped back for trivial ones. For every operator, a certain move probability is calculated and a random number is drawn from a uniform distribution. If the move probability exceeds this random number, the operator is changed. The move probability is calculated as described in the previous section according to the Metropolis-Hastings-alorithm. The underlying probability distribution here is given by the partition function. Naively one would assume firstly an operator at i, j is proposed with a proposal probability and then accepted with an acceptance probability. This process can be switched, firstly it is determined if any operator is inserted and after that the position of the operator is determined [39]. The proposal probability is therefore symmetrically 1. So the move probability can be calculated just by comparing the prefactors of the weight of the new configuration and the one of the old configuration.

$$p(1 \to H^d_{i,j}) = \min\left(1, \frac{\sum_{i,j} \omega\left(|\alpha\rangle, S'_\mathcal{L} = \{..., H_{i,j}, ...\}\right)}{\omega\left(|\alpha\rangle, S_\mathcal{L} = \{..., 1, ...\}\right)}\right) = \min\left(1, \frac{\beta \sum_{ij} |J_{ij}|}{2(\mathcal{L} - n(S_\mathcal{L}))}\right) \tag{52}$$

In this, the position of the operator to insert i, j does not matter at first, which is why the sum over all possible i, j is taken. The indices where the new operator is then really inserted are chosen at random from a pool of allowed positions weighted with their bond strength. For the long-range interactions along the legs, only the rung interactions, and the ones along the legs are allowed. For the $\mathcal{H}_\times$-model, all interactions are allowed ($[i, i]$ interactions are never allowed).

The probability to change a diagonal operator back to an identity operator is obtained in the same way:

$$p(H^d_{i,j} \to 1) = \min\left(1, \frac{2(\mathcal{L} - n(S_\mathcal{L}) + 1)}{\beta \sum_{ij} |J_{ij}|}\right). \tag{53}$$

At the end of each diagonal update, the filling of the sequence with non-trivial operators is checked, and if more than 75% of the operators are non trivial, the sequence is expanded by one trivial operator.

4.4.4 Off-diagonal update

The off-diagonal update is a non-local cluster update. In particular it follows the loop-update scheme described by Sandvik [39]. The given sequence of operators is traversed and connected with a loop at shared sites. Every loop has a $\frac{1}{2}$-chance of being flipped. Being flipped here means, that every time a loop which is flipped traverses trough an operator, the diagonal operator is changed to an off-diagonal operator and vice versa (see figure 4c, d). Every operator is traversed by two loops. This means in particular, that an operator traversed by the same loop twice or by two loops, which are both flipped stays the same. If a loop which is flipped traverses trough the periodic boundary condition of the configuration, the affected spins of the state $|\alpha\rangle$ are also flipped (see figure 4a, b).

A speciality that must be taken into account is, that in the long-range models investigated here ferromagnetic operators as well as antiferromagnetic operators show up, depending on the sites the operator affects. One can see from the examples in figure 4, that one has two ways of a loop traversing an operator. It can leave on the same side, that it entered or leave on the opposite side that it entered. When the loop is flipped it will flip all the spins it traverses, so the two spins on one side of the operator or the two spins on different ends of the operator. This is equivalent to changing the operator from diagonal to off-diagonal or vice versa in combination to changing the spins it loops over when leaving the configuration space on the top or bottom [39].

Theoretically, all ways to traverse an operator are possible, but the resulting changes in the spins must correspond to a matrix element of the Hamiltonian. The non-zero matrix elements are

$$\begin{aligned} &H_{ij} = H^d_{i,j} + H^{od}_{i,j} \\ &\langle\uparrow\uparrow| H_{ij} |\uparrow\uparrow\rangle = \frac{1}{4}J_{ij} \quad \langle\downarrow\downarrow| H_{ij} |\downarrow\downarrow\rangle = \frac{1}{4}J_{ij} \quad \langle\uparrow\downarrow| H_{ij} |\uparrow\downarrow\rangle = -\frac{1}{4}J_{ij} \\ &\langle\downarrow\uparrow| H_{ij} |\downarrow\uparrow\rangle = -\frac{1}{4}J_{ij} \quad \langle\uparrow\downarrow| H_{ij} |\downarrow\uparrow\rangle = \frac{1}{2}J_{ij} \quad \langle\downarrow\uparrow| H_{ij} |\uparrow\downarrow\rangle = \frac{1}{2}J_{ij} \end{aligned} \tag{54}$$

and the corresponding representations in the configurations are shown in figure 3a). From that, one can easily deduce which loop traversals are allowed in this model and which are not by checking if the resulting matrix element has non-zero weight.

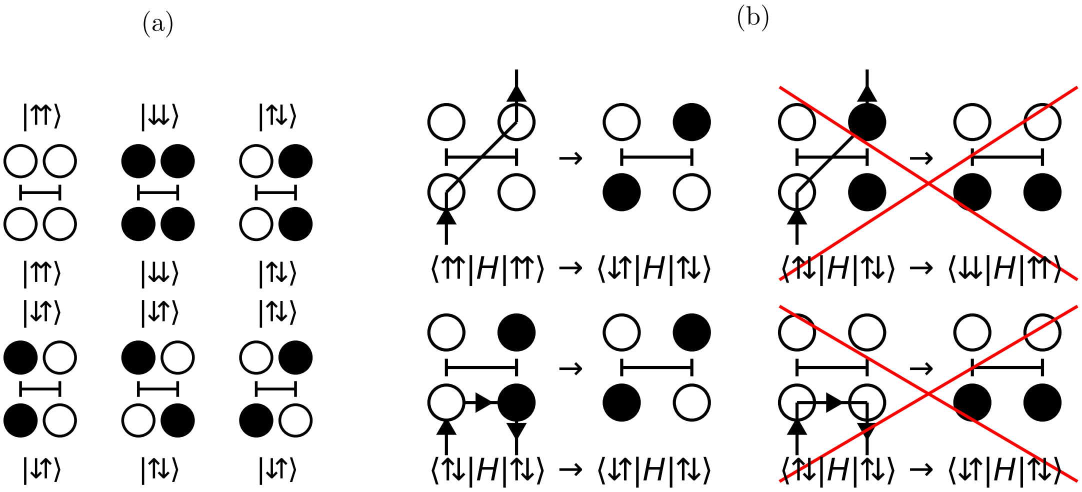

Figure 3: (a) Matrix elements with non-zero weight. (b) Examples of two resulting loop traversals which are allowed and two which are forbidden.

One finds, that when traversing an antiferromagnetic operator, the loop leaves the operator through the same side it has entered. When traversing a ferromagnetic operator it goes through the operator and leaves on the other side, this can also be seen in figure 3b).

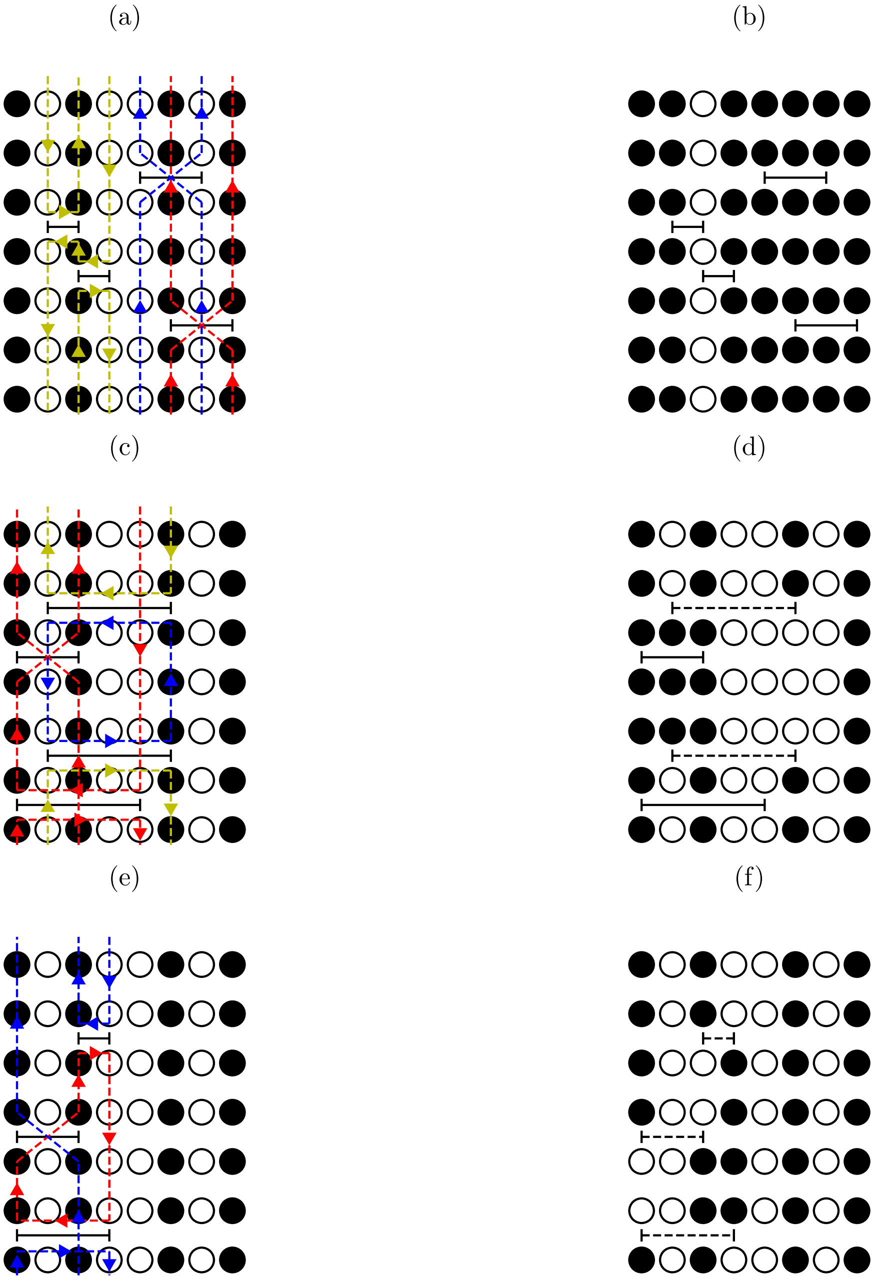

Figure 4: An exemplary SSE configuration for a parallel ladder with 4 rungs and therefore 8 sites.
(a) The sequence contains 4 diagonal operators at different sites. These operators form three loops, two of which will be flipped. Each of the affected operators is traversed by the same loops twice, so effectively no operators in the sequence are changed. The state $|\alpha\rangle$ however is changed, the spins crossed by the flipped loops are flipped as well. The resulting configuration after the loop update is shown in (b).
(c) Another configuration with three loops, where the blue one is flipped and therefore the two diagonal operators $H^d_{1,5}$ are changed to off-diagonal operators. These change the propagation of the state $|\alpha\rangle$ in imaginary time by flipping the two sites, shown in (d).
(e) An example configuration where ferromagnetic and antiferrmagnetic loop passings, the red loop will be flipped, the blue one wont. This results in the configuration shown in (f).

4.4.5 Observable Staggered magnetization

As aforementioned, the first observable one wants to measure is the squared z-component of the magnetization. It is given by

$$m_z^2 = \left(\frac{1}{L} \sum_{l \in \{0,1\}} \sum_{r=0}^{L/2-1} S^z_{lL/2+r} e^{i\pi(l+r)} \right)^2 \tag{55}$$

with summation over the legs l and rungs r of the ladder. The expectation value for this squared magnetization can be calculated via the partition function as [35]

$$\langle m_z^2 \rangle = \frac{1}{Z} \sum_{\{S_\mathcal{L}\}} \sum_{\{|\alpha\rangle\}} \frac{\beta^{n(S_\mathcal{L})}(\mathcal{L} - n(S_\mathcal{L}))!}{\mathcal{L}!} \langle\alpha| \, m_z^2 \prod_{p=0}^{\mathcal{L}-1} H_{a_p,b_p} |\alpha\rangle \, . \tag{56}$$

As another observable, the staggered magnetization to the power of 4 is calculated in the same way. With that the Binder cumulant will later be calculated.
From the squared staggered magnetization, the critical exponents β and ν will be calculated.

4.4.6 Observable Staggered susceptiblity

Another quantity which will be measured is the magnetic susceptibility based on the staggered magnetization from 4.4.5. In the derivation of the susceptibility [27] and [37] is followed. The susceptiblity can be defined as an integral over the imaginary time:

$$\chi = L \int_0^\beta \langle m(\tau) m(0) \rangle d\tau. \tag{57}$$

The integrand can be expanded in SSE as

$$\langle m(\tau) m(0) \rangle = \frac{1}{Z} \mathrm{tr} \left(e^{-\beta\mathcal{H}} e^{\tau\mathcal{H}} m e^{-\tau\mathcal{H}} m \right) . \tag{58}$$

Following the derivation from [27], the imaginary-time integral can with this be written as

$$\langle \chi \rangle = \frac{L}{Z} \sum_{\{S_\mathcal{L}\}} \sum_{\{|\alpha\rangle\}} \frac{\beta^{n(S_\mathcal{L})}(\mathcal{L} - n(S_\mathcal{L}))!}{\mathcal{L}!} \frac{\beta}{n(S_\mathcal{L})(n(S_\mathcal{L})+1)} \left[\sum_{p=0}^{n(S_\mathcal{L})-1} m_p m_p + \left\{ \sum_{p=0}^{n(S_\mathcal{L})-1} m_p \right\} \left\{ \sum_{p=0}^{n(S_\mathcal{L})-1} m_p \right\} \right] \tag{59}$$

with $m_p = m_z(|\alpha(p)\rangle)$.

4.4.7 Convergence to zero-temperature properties

In this thesis, the properties of the ground-states of the systems are to be investigated. Because SSE is a finite temperature method, it is not possible to sample the ground-state directly. But in contrast to the infinite system, the excitations above the ground-state are always gapped on finite systems. So to effectively sample the ground-state it is sufficient to choose a low enough temperature to be below that gap.

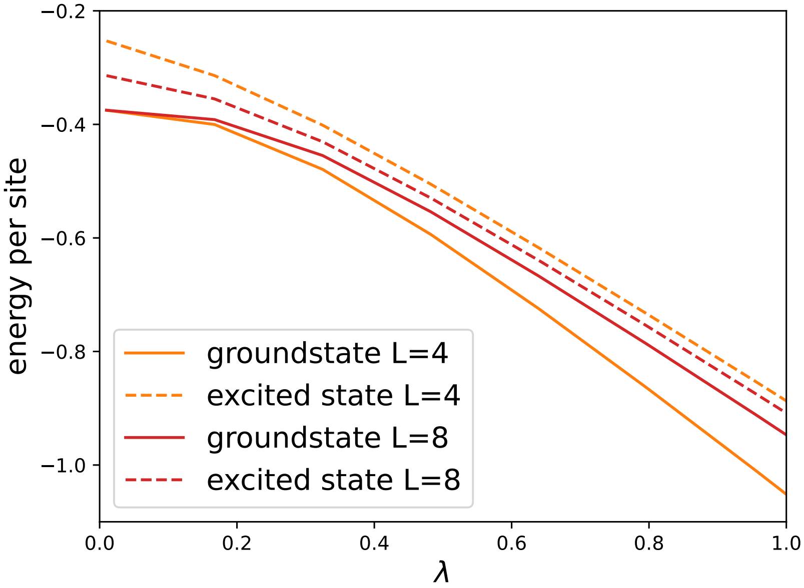

Figure 5: Energy spectra of the ground-state and first excited state for the $\mathcal{H}_{\parallel}$ model at $\sigma = 0.5$ for two different system sizes. Finite systems are always gapped and the gap shrinks for larger L. The gap stays finite for $L \to \infty$ in the rung singlet phase but closes in the Néel phase.

Here, the beta-doubling approach developed by Sandvik [39] is implemented. This means, the system is “cooled”, by increasing β and giving the system time to adjust. In detail, from the starting point $\beta = \beta_0$, it is doubled in every step k ($\beta = \beta_0 2^k$). Along with that, the sequence of operators is also doubled. Therefore, the sequence is mirrored and concatenated to itself:

$$S_{2\mathcal{L}} = \{[a_1, b_1], ...[a_{\mathcal{L}}, b_{\mathcal{L}}], [a_{\mathcal{L}}, b_{\mathcal{L}}], ..., [a_1, b_1]\} \tag{60}$$

Between the steps, the system is given a fixed amount of Monte Carlo steps to adjust. At the highest β the true sampling for the observables is then performed. This highest β is determined by looking at the convergence of the observables during the doubling (shown in Fig. 6) and choosing, at which β the observables are converged.

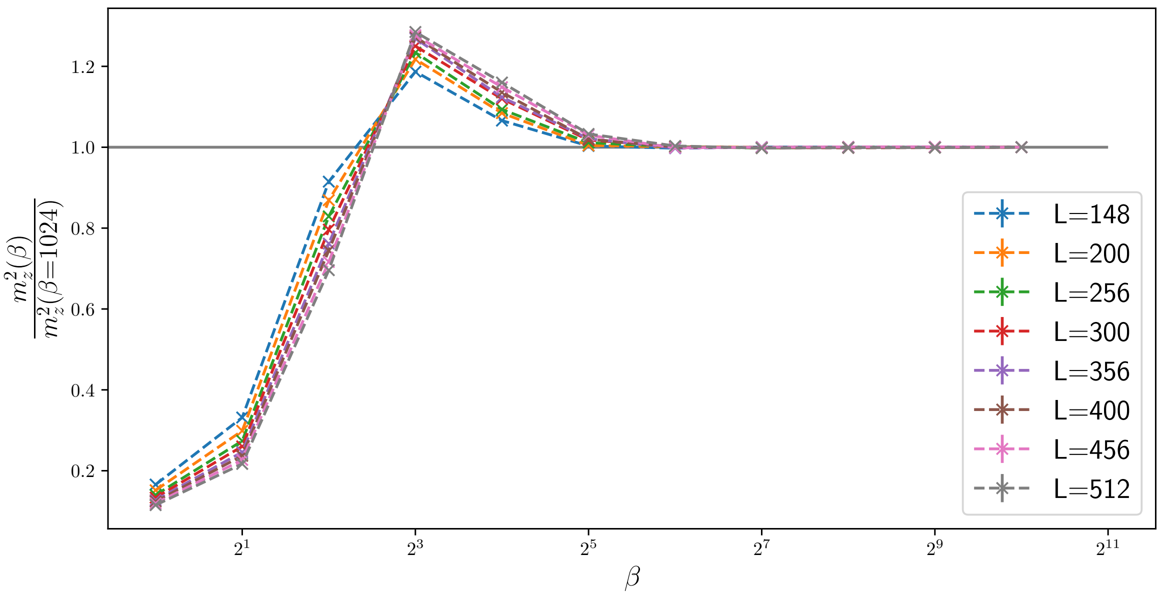

Figure 6: Convergence of the squared staggered magnetization in the beta-doubling scheme evaluated close the critical point of the $\mathcal{H}_\times$-model for $\sigma = 0.5$.

4.5 Finite-size effects

4.5.1 Challenges from finite-size effects

In this thesis, the critical points as well as critical exponents of the phase transitions described before will be determined. These properties are defined in the thermodynamic limit, but with the SSE scheme used here it is only possible to sample systems of finite scale.

But one can still determine the critical properties of the infinite system by looking at the behavior of the finite counterpart. Instead of singularities at the critical point, the quantities of interest are continuous in finite systems. In the case of the susceptibility for example, there is only a peak in the finite system, where a singularity should be in the infinite system. This peak is then shifted and rounded as the system size changes [13]. These deviations set in, when the correlation length ζ hits the system size L as it diverges at the critical point. It makes intuitive sense that how fast the quantities diverge has an effect to how they are rounded in the finite system. So these deviations can be connected to the critical exponents of the infinite system [10]. One sees, that the exponents can be extracted by investigating the phase transitions on finite systems of different scale.

4.5.2 Finite-size scaling

In this section the explanations in [28] and [13] are followed.

To understand how the critical exponents influence the scaling of finite systems, one has to look at the field theoretical ansatz for the free energy. As described in sections 2.1 and 3.4, the free energy functional and other thermodynamical potentials can be rescaled by a factor k to different powers for the different dependencies. The free engery in terms of r, u, external field H and system size L obeys

[28]:

$$f(r,u,H,L^{-1}) = k^{-(1+z)} f(k^{[r]}r, k^{[u]}u, k^{[H]}H, kL^{-1}). \tag{61}$$

Below the upper critical dimension, u is set to zero and with $k = L$ one obtains the scaling behavior of the magnetization by differentiating the free energy by H:

$$m(r,L^{-1}) = \frac{\partial f}{\partial H}|_{H=0} = L^{[H]-(1+z)} f(L^{[r]}r, 1). \tag{62}$$

With [28]

$$\beta = \frac{1+z-[H]}{[r]} \text{ and } \nu = [r]^{-1} \tag{63}$$

one obtains

$$\begin{aligned} m_L(r) &= L^{-\beta/\nu}\Psi_m\left(L^{1/\nu}(r-r_c)\right) \\ m_L^2(r) &= L^{-2\beta/\nu}\Psi_{m^2}\left(L^{1/\nu}(r-r_c)\right), \end{aligned} \tag{64}$$

where Ψ is the universal scaling function of the magnetization m [28], which will be a high-order polynomial for the evaluation of the numerical data.
By the same logic, one obtains for the scaling of χ:

$$\chi_L(r) = L^{\gamma/\nu}\Psi_\chi\left(L^{1/\nu}(r-r_c)\right). \tag{65}$$

Above the upper critical dimension, this scaling has to be supplemented with a pseudo critical exponent koppa ($\koppa$) [28].

$$\koppa = \max\left(1, \frac{d}{d_{uc}}\right). \tag{66}$$

With $\koppa$ the scaling for magnetization and suscebtibility can be generalized to [28]:

$$\begin{aligned} m_L^2(r) &= L^{-2\beta\koppa/\nu}{\Psi'}_{m^2}\left(L^{\koppa/\nu}(r-r_c)\right) \\ \chi_L(r) &= L^{\gamma\koppa/\nu}{\Psi'}_\chi\left(L^{\koppa/\nu}(r-r_c)\right). \end{aligned} \tag{67}$$

This also changes the hyperscaling relation (7) to [28]

$$2-\alpha = \left(\frac{d}{\koppa}+z\right)\nu. \tag{68}$$

With (23), equation 66 can be rewritten to give an explicit formula for $\koppa$:

$$\koppa = \max\left(1, \frac{2}{3\sigma}\right). \tag{69}$$

So $\koppa$ will be $\frac{2}{3\sigma}$ for $\sigma < \frac{2}{3}$ and 1 for $\sigma \geq \frac{2}{3}$.

4.5.3 Data collapse

In the following description of the data collapse we used, Ref. [22] is followed.

With the scaling formulas (67), one can determine the critical point λ_c and the critical exponents ν, β and γ from the SSE Monte Carlo data. To map out the whole phase diagram in λ and σ direction, for a fixed σ, the observables are simulated for a set of different λ. For each of these "slices", simulations at different system sizes L are performed. The critical behavior can be determined by performing a two-dimensional fit of the scaling formulas over the λ and L axes.

Rescaling the observable and the λ-range with the determined critical point and the exponents should now map all the system sizes onto each other. The qualitiy of the critical point and exponents is dominated by how well the curves map onto each other, as well as the rescaled λ range being symmetrical around zero ($\lambda_c = 0$ in the rescaled space).

This process is then repeated multiple times for the same σ value, where the new λ range for each run is determined by performing an inverse scaling with the critical point and ν from the last run. Two example runs are shown in figure 7. This should then quickly converge to where all data sets lie perfectly on each other, which marks the critical values that are taken for further calculations. To get statistics on these values and determine a meaningful uncertainty, this scheme is performed multiple times for different seeds and the mean and standard error of the desired values over the seeds is calculated.

4.5.4 Identifying the critical point from Binder ratios

This data collapse scheme can only be applied when varying λ at a fixed σ, but for higher σ values data slices with varying σ at a fixed λ were also taken. Looking at these phase transitions one can determine the critical point by Binders method described in [4]. This works well but per se does not yield information about the critical exponents. In [42], the authors were able to determine the critical exponents ν and z from Binder ratios.

Regarding the critical point, it was here determined by identifying the crossings of Binder ratios (defined in Eq. 70) for different system sizes. The Binder ratios are defined by

$$B = \frac{3}{2}\left(1 - \frac{1}{3}\frac{\langle m_z^4\rangle}{\langle m_z^2\rangle^2}\right) \tag{70}$$

In particular the crossings of one system of size L and the other of size $2L$ were taken into account. To extrapolate the critical points obtained by this to the thermodynamic limit, a power law fit (Eq. 71) was used to determine the critical point of an infinite system at $1/L \to 0$ (see Fig. 8).

$$\sigma_c(L) = \sigma_c(L = \infty) + \frac{b}{L^a} \tag{71}$$

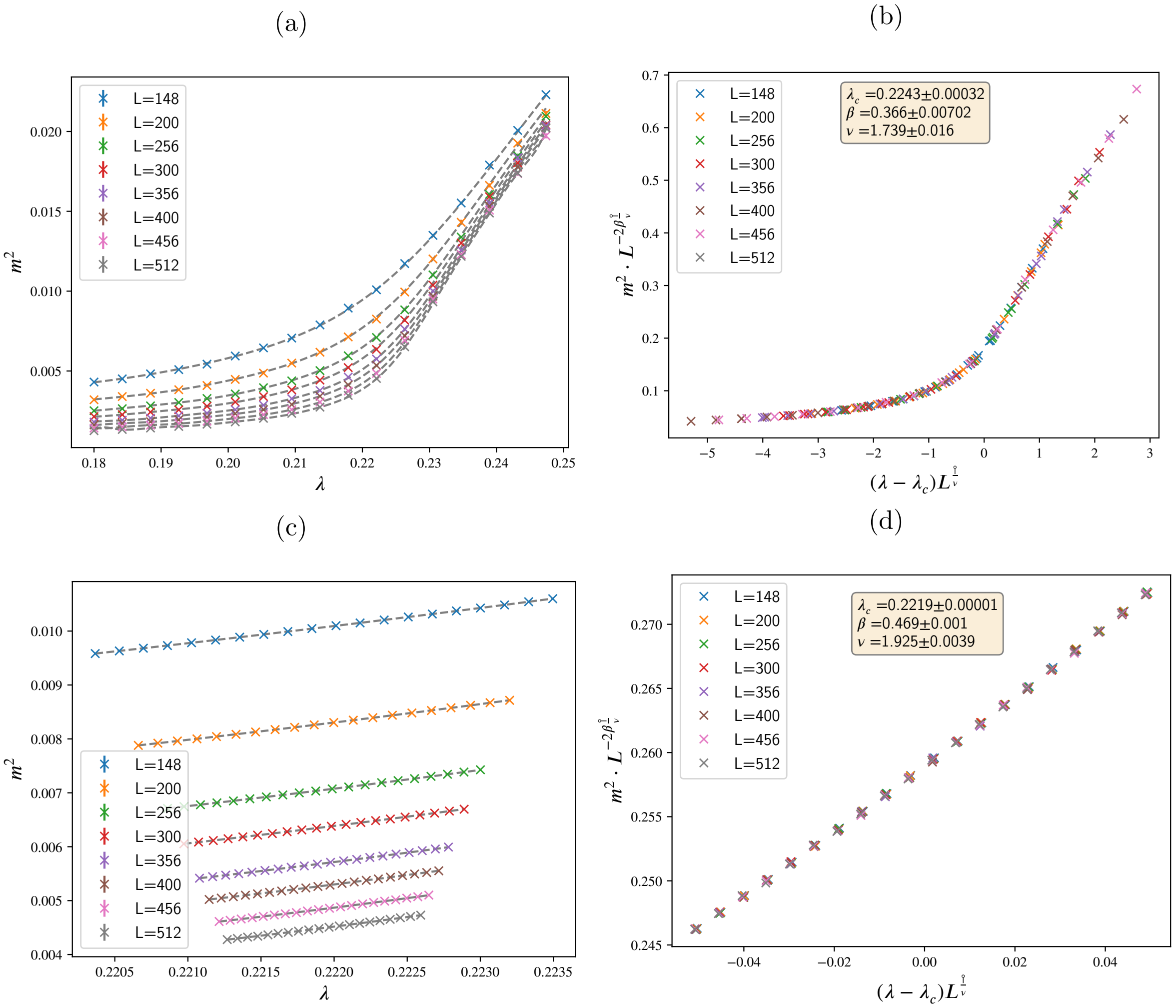

Figure 7: Different data collapse runs of the squared staggered magnetization of the $\mathcal{H}_{\parallel}$-model at $\sigma = 0.5$.
(a) Magnetization data over λ in a relatively wide range around an initial guess of λ_c, with the respective fit curve.
(b) Collapsed magnetization data of that initial wide λ range, the data points are scattered and the λ range is not centered. The resulting λ_c and exponents are given.
(c) Magnetization data of a narrow λ range inversely scaled by previously determined λ_c and exponents with their respective fit curve.
(d) Collapsed magnetization data of the narrow λ range, the rescaled data points fall very close onto each other and the λ range is very symmetric around zero. One can see, that the λ_c and exponents are better than in (b) as they are closer to their expected value and the fit error is much smaller.

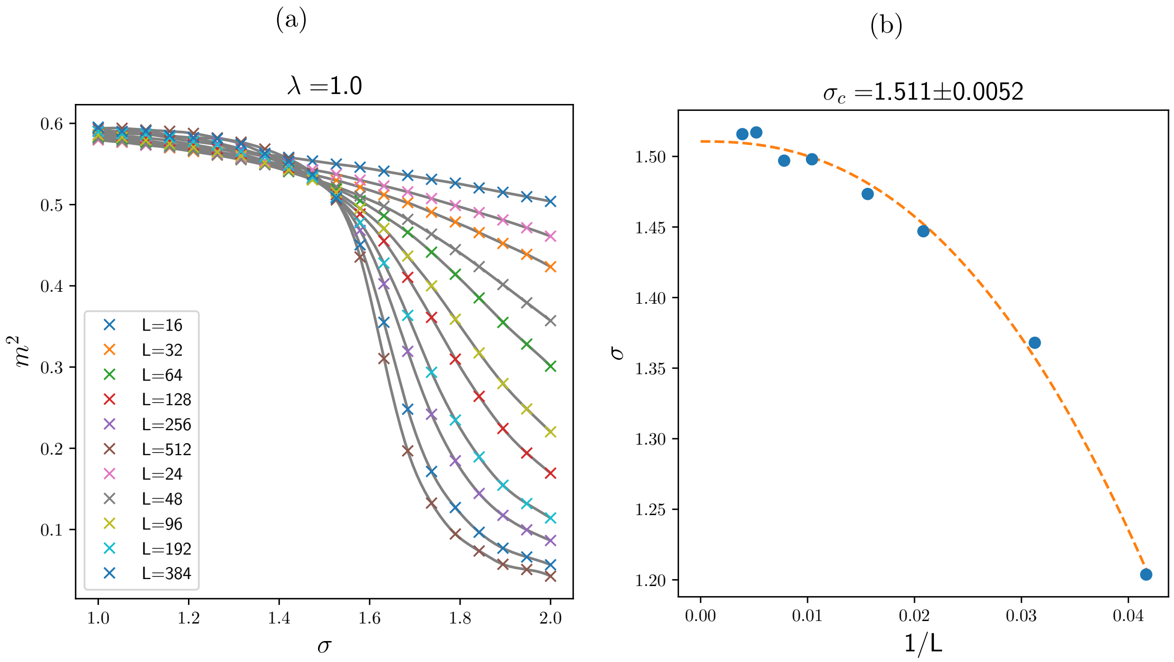

Figure 8: (a) Interpolated Binder ratios of the $\mathcal{H}_\times$ model at $\lambda = 1$ for different values of σ. (b) Crossings of the Binder ratios with power-law fit over inverse system size.

Furthermore, the critical exponent ν can also be extracted from the Binder ratios, in particular from the derivative of the Binder ratios at the respective critical point [42]

$$\nu_c(L) = \left[\log_2 \frac{\partial_\sigma B(\alpha_c(L), L)}{\partial_\sigma B(\alpha_c(L), 2L)}\right]^{-1} . \tag{72}$$

This will not be used, since the numerical differential needed for this makes it difficult to get exact results for ν. Once the critical point is determined, β and γ can be determined up to a factor of $1/\nu$, by looking at the L-scaling at the critical point given by (67):

$$\begin{aligned} m_L^2(r_c) &= L^{-2\beta\text{♀}/\nu} {\Psi'}_{m^2}(0) \\ \chi_L(r_c) &= L^{\gamma\text{♀}/\nu} {\Psi'}_{\chi}(0) \, . \end{aligned} \tag{73}$$

Using the slope of this scaling in a double logarithmic plot, one can determine the exponents of L and therefore β/ν and γ/ν.

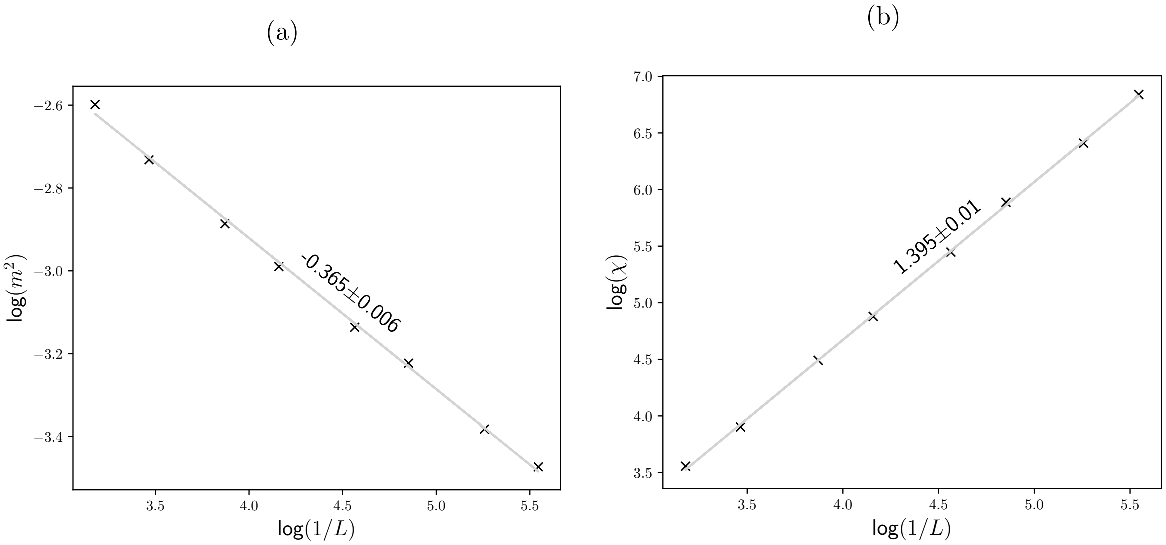
(a)

(b)

Figure 9: (a) The slope of the magnetization scaling in a double logarithmic plot derived from the same data set as in figure 8. (b) The slope of the susceptibility scaling in a double logarithmic plot derived from the same data set.

5 Results for the antiferromagnetic long-range Heisenberg ladder

So far, the models investigated in this thesis and the methods by which their properties will be determined were discussed. With the quantum Monte Carlo SSE method the three observables squared staggered magnetization, staggered magnetization to the fourth power and the susceptibility were sampled. And finite size methods like the data collapse and Binder ratios can be used to deduce the properties in the thermodynamic limit from finite length systems.

In the following, using all of these methods, the quantum phase diagrams of the two antiferromagnetic long-range Heisenberg ladders are mapped out. The phases and limiting cases can be verified and the detailed properties of the phase transitions in the form of critical exponents are investigated. The results we present in the following, calculated for the first time using QMC methods, will be compared and verified by data on these models determined by other methods. We will also discuss the limitations of the method and the problems we faced.

5.1 Phase diagrams

The critical points for both ladder models were determined by the aforementioned data collapse as well as Binder ratio methods. For small σ data collapses were performed for a fixed σ. From the quantum phase diagrams in figure 10 and 11 one can see, that the critical point shifts to larger λ_c linearly with σ, for larger σ λ_c deviates from that behavior. This is the case for $\sigma \gtrapprox 0.8$ on the parallel ladder, and for $\sigma \gtrapprox 1.1$ on the cross ladder. This difference was also observed with the pCUT method [1] and can be attributed to the cross leg interactions strengthening the Néel order.

Above a certain σ, data collapses at a fixed σ will not work anymore, on which we will elaborate in section 5.3. There, Binder ratios were used at a fixed λ to determine the respective critical σ_c. This method was used to map out the phase transition for more λ values.

In the linear regime at small σ, the QMC data fits the pCUT data [1] very well, the critical points could be reproduced nearly perfectly. As the σ values increase, the two methods deviate more from each other. In particular, the pCUT λ_c rises earlier than the QMC λ_c. This is even more evident for the cross ladder $\mathcal{H}_\times$, where the pCUT data lies clearly above the QMC data for bigger σ. It must be noted though that the singular point from [42], also calculated with QMC methods fits more closely to the QMC data presented here. Overall it seems, that the pCUT data tends to overshoot the critical values at higher σ.

One can see, that the spin wave data [1] is in good agreement with the QMC critical points. For small σ, the spin wave λ are clearly below all other data, at higher σ it grows faster than the other critical points and gives a sharper right edge to the Néel phase. This is true for both the parallel and the cross ladder. Regarding the spinwave calculations (see section 3.5) one can perform a large λ approximation to get critical σ^{SW} values for $\lambda \to \infty$ [1]. The deviations of the spin wave data to the QMC results can be explained by the linear spin wave calculations being a rather rough approximation but a good qualitative intuition. It is not clear though, why the spin wave data lies left of the QMC σ for $2.5 \lessapprox \lambda < \infty$ and right of the QMC data for $\lambda = \infty$. This would suggest, that the QMC data for $2.5 \lessapprox \lambda < \infty$ should be shifted to lower σ to be consistent there.

Other works [6, 9] suggest, that the critical σ converges to a finite value at $\lambda = \infty$. In other words, no long-range (Néel) order exists above a certain σ. To investigate this, the critical points at $\lambda = \infty$ were also calculated with the QMC method in this thesis for both models.

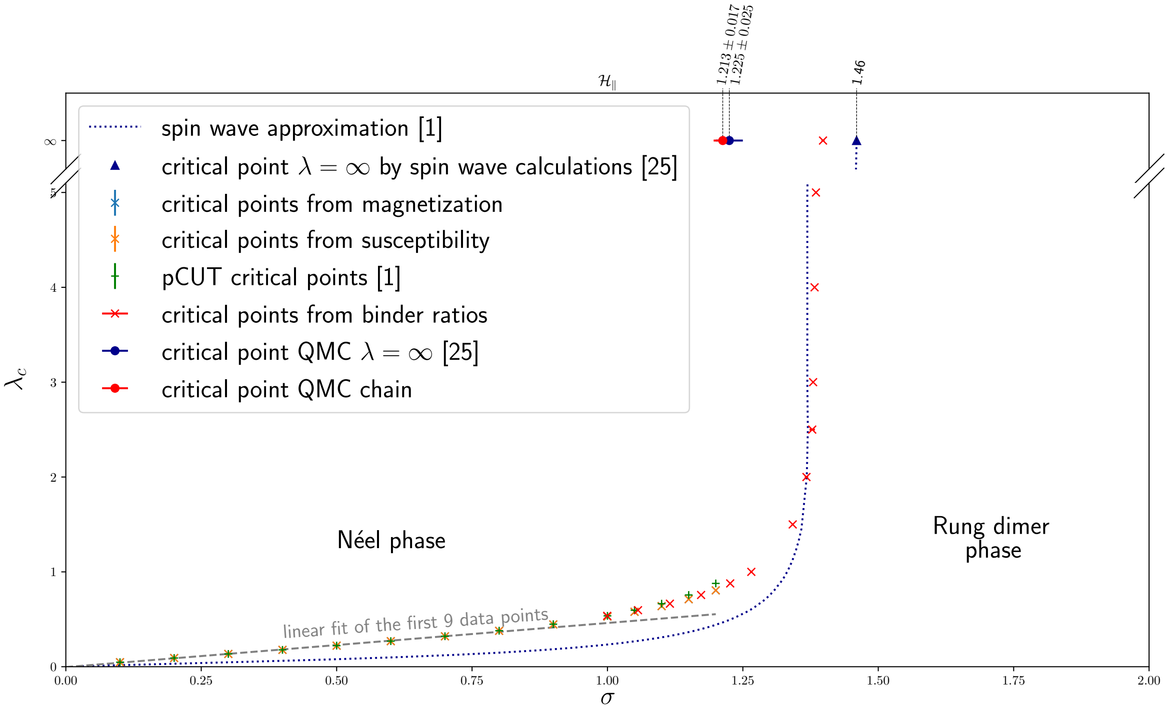

Figure 10: Phase diagram of the ladder with long-range interactions along the legs. The transition between the Néel phase and the rung dimer phase is shown with the approximation by linear spin waves [1]. The QMC data derived in this thesis is shown, as well as pCUT data [1] for comparison. For $\lambda \to \infty$, critical σ values from [25] are also given.

The critical σ at $\lambda = \infty$ for the ladders cannot be calculated naively by setting $J_\perp = 0$, a small $J_\perp$ ineraction has to always be active to guarantee an antiferromagnetic coupling of the chains. The naive approach is only possible in the parallel ladder, where the two chains decouple. We can modify our simulation to sample only the antiferromagnetic long-range Heisenberg spin-$\frac{1}{2}$ chain. The σ_c derived from this is also included in the phase diagram of the parallel ladder 10.
To approximate the limiting $\sigma_c(\lambda = \infty)$ of the two ladder models, $J_\perp$ is set to 1 and σ_c for higher and higher λ values is determined. We then investigate to which value the critical σ will converge for $\lambda \to \infty$. This process is shown for $\mathcal{H}_\parallel$ in figure 12 and for the $\mathcal{H}_\times$-ladder in figure 14.

One notices, that for the parallel ladder lower values of λ (up to $\lambda = 30$) are used. It must be said here, that the crossings of the Binder ratios are more difficult to determine for high values of λ. In particular, the crossing points shift away from the critical point for higher λ but towards the critical point for larger system sizes (figure 13). It seems like the higher the λ, the larger the system must be to determine the critical point correctly. This makes sense, since for higher λ the long-range interactions are stronger and "feel" the limitation of the finite system faster as the chains decouple. For the ladder with cross leg long-range interactions the chains do not decouple for $\sigma < \infty$ and therefore this problem is not present.

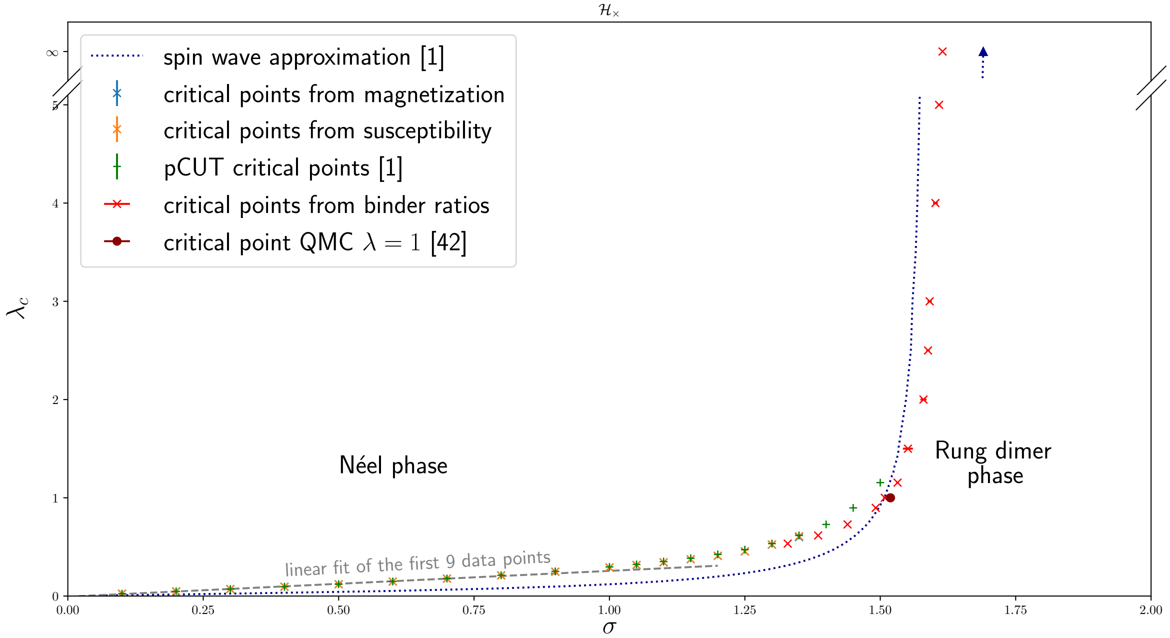

Figure 11: Phase diagram of the ladder with long-range interactions across the legs. The transition between the Néel phase and the rung dimer phase is shown with the approximation by linear spin waves [1]. In addition to the QMC data, pCUT data [1] of the quantum phase transition is also given, as well as a quantum critical point from [42] for comparison.

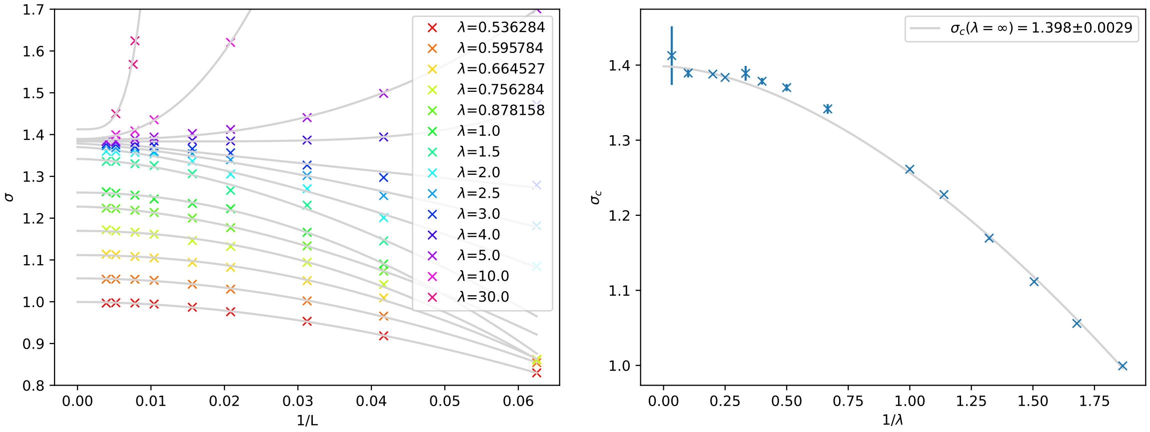
(a)
(b)

Figure 12: Determination of $\sigma_c(\lambda = \infty)$ for the parallel ladder.
(a) σ crossings of the Binder ratios for different λ with equation (71) fits. (b) extrapolation of the σ_c to $\lambda \to \infty$ by also applying a power law fit.

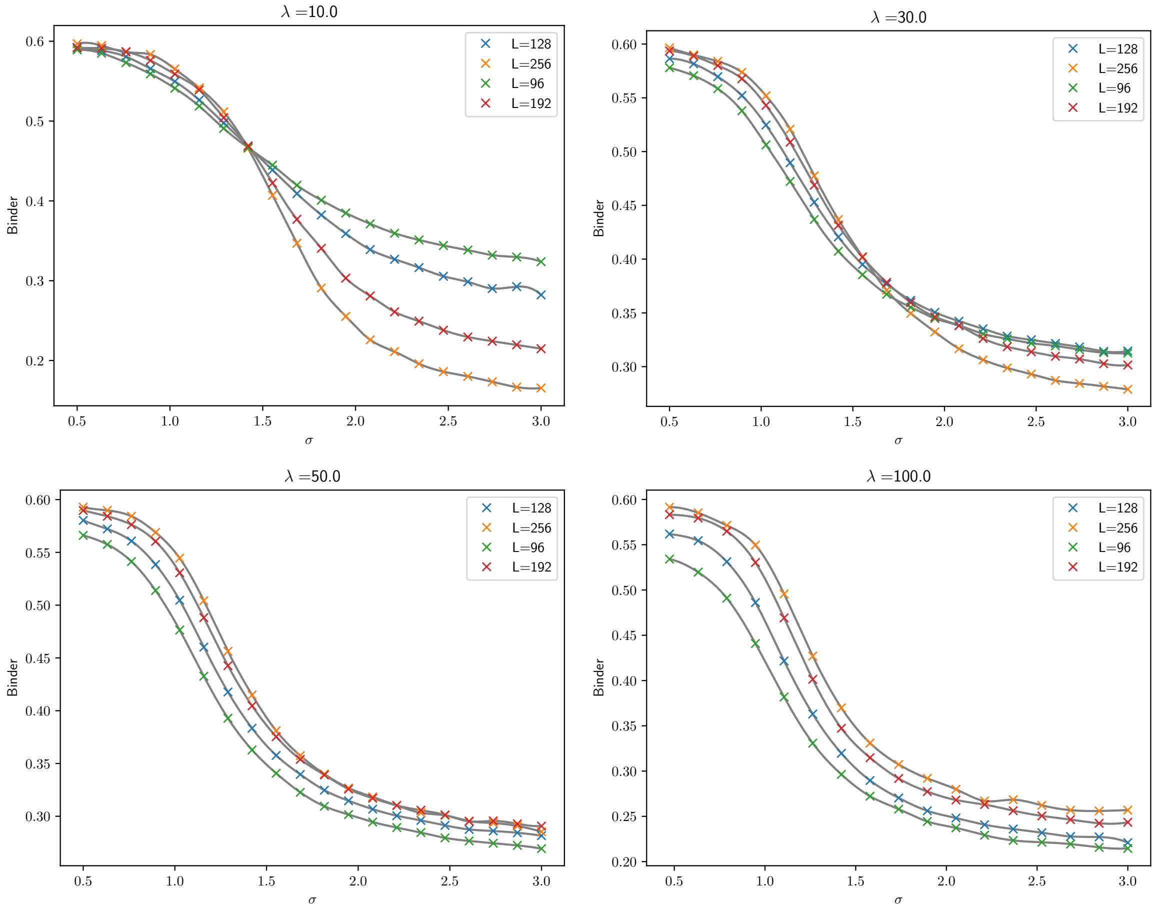

Figure 13: Binder ratios of four different system sizes for the parallel ladder at different values of λ. A shift in the crossing points is clearly visible until at $\lambda = 100$, the ratios do not cross anymore in the σ-range investigated.

A comparison for the $\mathcal{H}_\parallel$-ladder in the limiting case $\lambda = \infty$ can be drawn from [25]. The model investigated there is a spin-$\frac{1}{2}$ antiferromagnetic long-range chain. Since quantum phase transitions are universal and therefore do not depend on the overall energy scale of the Hamiltonian, equation 10 can be rescaled by $1/\lambda$:

$$\frac{\mathcal{H}_\parallel}{\lambda} = \mathcal{H}'_\parallel = \sum_i \frac{J_\perp}{\lambda} \vec{S}_{i,1} \cdot \vec{S}_{i,2} - \sum_{i,\delta>0} \sum_{n=1}^{2} \frac{(-1)^\delta}{|\delta|^{1+\sigma}} \vec{S}_{i,n} \cdot \vec{S}_{i+\delta,n}. \tag{74}$$

And in the limit $\lambda \to \infty$, one finds a correspondence to the Hamiltonian in [25]:

$$\mathcal{H}'_\parallel(\lambda \to \infty) \propto \mathcal{H}^{[25]}. \tag{75}$$

Therefore, the critical points from [25], obtained by QMC methods and spinwave calculations are included in the phase diagram (Fig. 10). One can see, that the $\lambda = \infty$ approximation from the QMC method in this thesis fits between the two. In particular, it fits more closely to the spin wave data, whereas the QMC point from [25] is at a lower σ. For comparison, we also determined the critical σ of a spin-$\frac{1}{2}$ chain with QMC and the point lies very close to the one from [25], even though the system sizes studied in [25] are up to four times as high as in the studies here. As described, one expects the two models to be continuously connected when tuning λ, so the $\lambda = \infty$ point of the ladder, coming from the high λ limit as discussed above, can not be accurate. The most likely scenario is that the extrapolation of the $\lambda = \infty$ point does not yield the right value, because of the λ values chosen. As described, here a technical limit is present in which λ can be evaluated with the ladder size 512.

One can see in figure 12a, that the behavior of the Binder crossing points changes qualitatively. Up to $\lambda = 3$, the crossing points shift to lower values for smaller systems and to higher values for larger systems (the curves approach $L \to \infty$ from below). Above $\lambda = 3$, the critical points at $L \to \infty$ are approached from above and as described, the crossing points shift to higher values for smaller systems. For now, an algebraic relation (71) is assumed to fit the data, which forces the curves to converge. But for $\lambda = 30$, this fits the data not as well and assuming other models, the critical σ could as well be estimated to be much lower. The value for subsequent λ could then approach the spin-$\frac{1}{2}$ chain value for σ_c.

That behavior would correspond to the critical points in the quantum phase diagram shifting more to the left above a certain λ, although this is not regarded in spin wave calculations and does not seem to fit to the behavior of the quantum phase diagram at lower λ, a strong indication for that being the case is the aforementioned change in behavior in figure 12a.

This also raises the question, if the utilization of horizontal slices at a fixed λ is justified for determining the correct critical points, since the scaling behavior in λ described in earlier sections does not necessarily hold in the case of varying σ from the theory. A systematic error, that shifts the critical points to higher σ can not be ruled out here.

For the limiting case $\lambda = \infty$ on the ladder with cross leg interactions, the ladder does not decouple for $\sigma < \infty$, because the interactions between the legs scale also with λ, so the bonds are only strengthened with growing λ. Because of the stronger coupling of the chains in the high λ limit, the crossing points of the Binder ratios are more well-behaved even for much higher λ. In both cases one can see, that there indeed is a σ_c above which no long-range order exists, but its value depends on the model. Whereas other works [6, 9] suggest an upper limit of $\sigma_c = 2$, in this thesis upper bounds of 1.398 ± 0.0029 and 1.615 ± 0.0014 were found respectively for the different ladders. This is also confirmed by pCUT and spin wave calculations [1, 25]. One can conclude that the upper limit of σ above which no long-range order exists depends strongly on the geometry and the interactions of systems investigated.

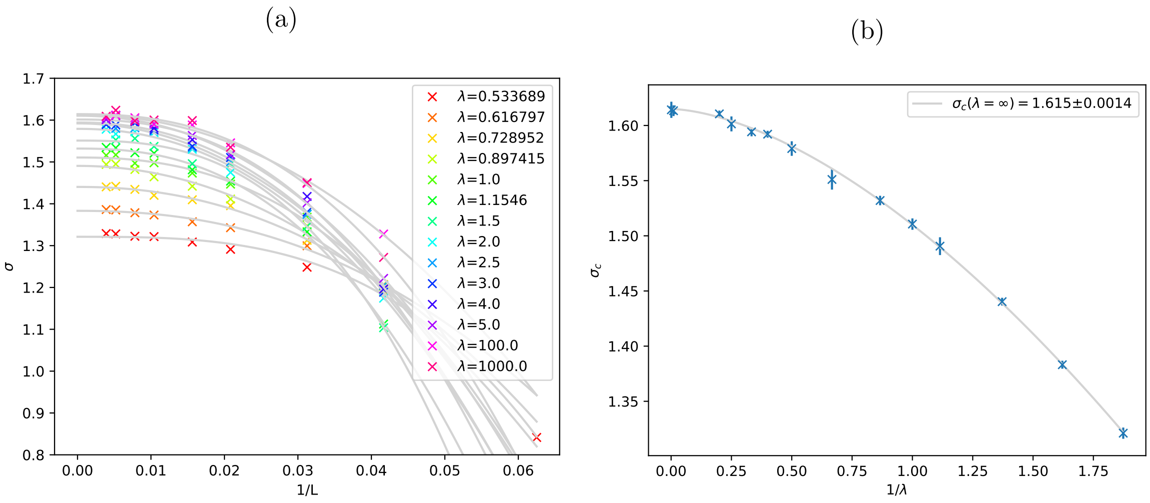

Figure 14: Determination of $\sigma_c(\lambda = \infty)$ for the cross ladder.
(a) σ crossings of the Binder ratios for different λ with Eq. 71 fits. (b) extrapolation of σ_c to $\lambda \to \infty$ by also applying a power law fit.

5.2 Critical exponents

In addition to the quantum phase diagram, the critical exponents characterizing the phase transition were investigated. As described before, the critical exponents ν, β and γ from the observables magnetization and susceptiblity were determined for every σ. From these three one can calculate all other exponents from the scaling relations (Eq. 5-7), even though the uncertainties on the exponents get amplified in this process. The results are shown in figure 15, in addition to the three "naturally" derived exponents $1/(z\nu)$ is calculated as well as β/ν and γ/ν.

This is due to a limitation one has, when evaluating the phase transitions at high σ derived from Binder ratios. Here β/ν and γ/ν can be determined from evaluating the observables at the critical point in a double log plot, using the relations 67. To infer β and γ one has to know ν. Although ν can also be derived from Binder ratios [42] in theory, in practice this proofed to be not sufficient due to the numerical derivative needed for that. To be able to compare the results from the higher σ phase transitions, all comparison data is divided by ν for the two lower right tiles in figure 15.

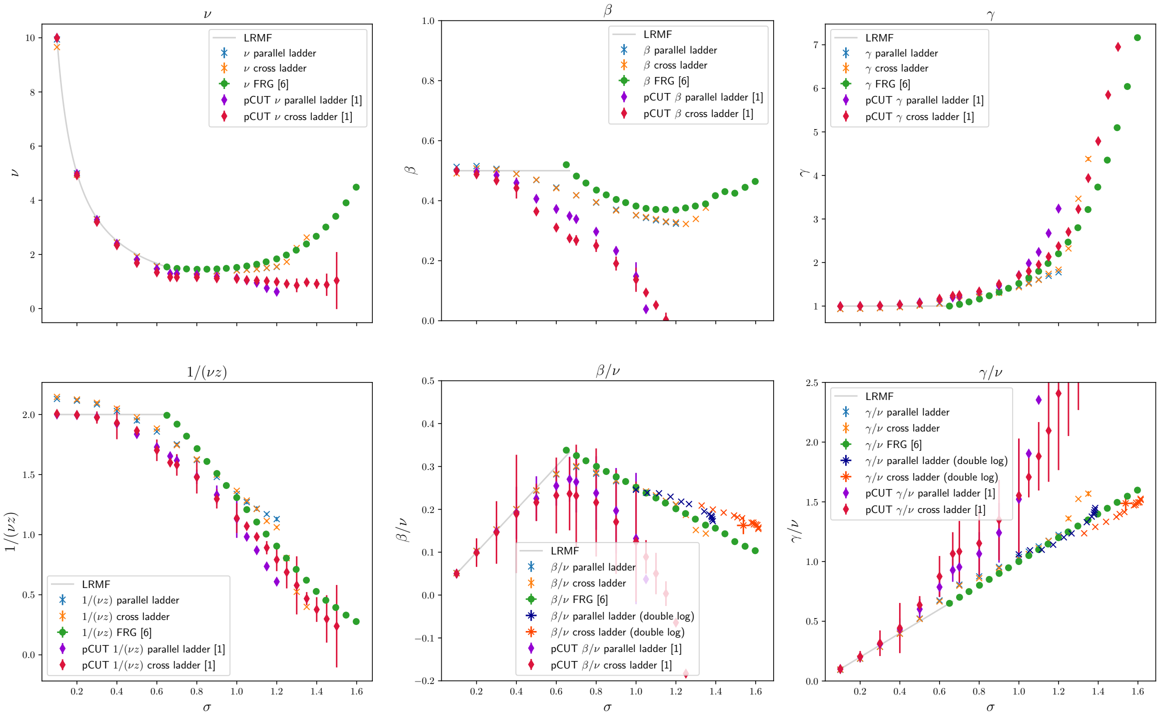

Figure 15: Measured critical exponents for the parallel and cross interaction ladders, with long-range mean field, pCUT and FRG comparisons.

In the plots, the long-range mean field (LRMF) expectations from sec. 3.4 are given and one can see, that the QMC data, as well as the pCUT [1] follow this prediction quite well. One expects corrections to the LRMF approaching the d_{uc} and therefore a deviation, which is present in the QMC and pCUT data, especially for β and γ.

Leaving the mean field regime, Ref. [6] provides a theoretical expectations derived from functional renormalization group (FRG). The pCUT ν seems to take on a constant value, as the FRG data rises for larger σ, here the QMC data fits this prediction more closely. $1/(z\nu)$ is included in this, as it is the exponent directly given in [6] together with $1/\nu$, from these the other FRG predictions are calculated using the scaling relations and $\eta = 2 - \sigma$. Because of that $1/(z\nu)$ is best suited for comparisons with FRG data.

Here the pCUT data matches the FRG data well and the QMC data is also consistent with the FRG $1/(z\nu)$. Turning to the two directly accessible QMC exponents β and γ, for comparison these are calculated from the pCUT and FRG data with the scaling relations. The pCUT β goes downwards after the mean field regime and takes on non physical negative values for large σ. The FRG β lowers and then rises again for larger σ, forming an arc shape, which is consistent with the QMC data. Here at least the cross ladder also performs this arc behavior. To investigate this further, one can turn to the β/ν data, which includes values for higher σ.

In this view, the FRG data is a straight line away from MF and it is closely followed by the QMC data collapse data as well as the double log plot data. Although the two QMC exponents differ quite a bit from each other, the FRG data lies between the two. One would assume that the exponent from double log plots overshoots the real value, looking at the overlap of it and the data collapse.

Evaluating the critical exponent γ all data sets follow a very similar upwards trajectory and only small deviations can be observed. The pCUT γ grows faster than both the FRG and QMC data, this becomes more clear in the γ/ν plot, where the pCUT data overshoots the other two. The QMC data over all is consistent with the FRG expectations, where the double log exponents undershoot a bit for the cross ladder. One can also see an overestimation at the last points of the data collapse QMC data, which is likely to the method breaking down there as described before.

5.3 Data collapse limitations

As mentioned before, the data collapse scheme does not work above a certain σ. For the parallel ladder, this never occurs, because the maximal σ is too low and one never enters this regime. In the cross ladder the maximum σ is around 1.6 and the data collapse breaks down at around $\sigma \approx 1.4$. below that, the data collapse works as described in section 4.5.3. For more iterations and a narrowing of the λ-range, the critical point and the exponents converge to their respective values. The "breaking down" of this method is characterized by these values not converging when performing more and more iterations, instead giving unphysical values, which are highly sensitive to the chosen λ-range. The difference becomes apparent, when looking at the stability of the critical properties when changing the λ-range shown in figure 16.

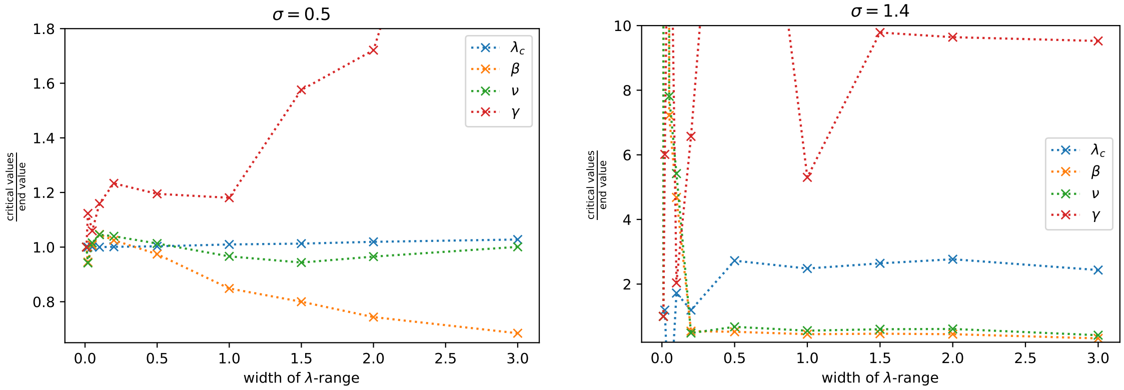

Figure 16: Critical properties of two phase transitions at $\sigma = 0.5$ and $\sigma = 1.4$ determined with data collapses based on different λ-ranges. It is apparent, that for $\sigma = 0.5$, the properties converge for small ranges, whereas the behavior of the $\sigma = 1.4$ system is not as well-behaved.

An indication on why the data collapse is not well-behaved at higher σ is, that the order parameter of the staggered squared magnetization does no longer behave as expected. As described before, one expects the order parameter being zero in the disordered phase and deep in the long-range ordered

phase should take on a value of $\frac{1}{3}\left(\frac{1}{2}\right)^2 \approx 0.08$, as only the z-component is evaluated.
In figure 17 one can see that this is the behavior for smaller σ but it does not work for σ above 1.4. For different system sizes the value in the ordered phase differs, the smallest system with $L = 8$ overshoots the expectation and takes on a value of ≈ 0.1. The larger the system, the lower the magnetization value in the ordered phase, for $L \to \infty$ the magnetization tends to zero. This indicates, that in the infinite system no phase transition occurs here.
It must be mentioned, that the usage of Binder ratios also does not yield a result for a critical point as the ratios do not cross anymore in the σ-range investigated.

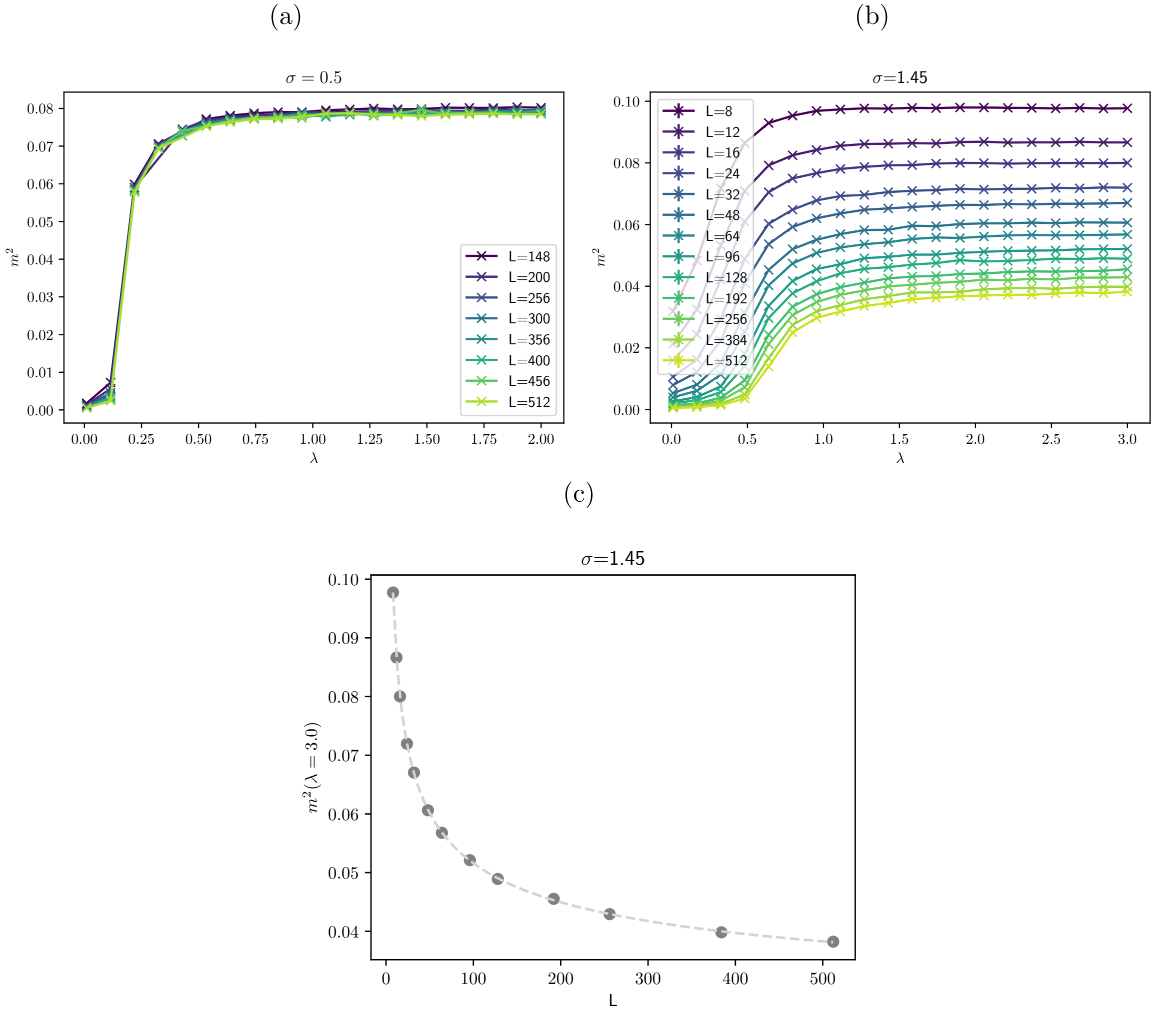
(a)
(b)
(c)

Figure 17: The squared staggered magnetization on a wide λ-range on the cross ladder at $\sigma = 0.5$ (a) and $\sigma = 1.45$ (b). For the smaller σ all systems take on the same value in the ordered phase, for the high σ, differently sized systems take on very different values in the ordered phase and the magnetization deep in that phase even tends to zero for larger systems, which is validated with an algebraic fit (c).

An interpretation of that could be that for those larger σ the QMC sampling takes place too close to the sharp edge in the quantum phase diagram. The proximity of the phase transition to the right edge of the phase has an effect on the magnetization which disturbes the data collapse and Binder ratios. This is backed by looking at this sharp phase transition edge at the right in figure 18. Particularly the phase transition is not sharp at all, although it seems to get sharper for larger systems, the magnetization drags slowly from zero to its expected value. At $\sigma = 1.45$, where no determination of λ_c is possible because of the deviations of the magnetization in the ordered phase (see Fig. 17), one can see in Fig. 18, that this deviation is caused by the phase transition in σ. In relation to the broadness of that phase transition, $\sigma = 1.45$ is rather close to the σ-limit of ≈ 1.6, even though it is still ≈ 0.15 units away.

It is not clear however, why this interpretation would not apply to the parallel ladder also. As mentioned the breakdown of the data collapse is not present there, so a fundamental difference must exist, that prevents this. One could speculate, that for the cross ladder one would need larger systems to avoid this issue, since the system "feels" its limitation more with more long-range interactions, so larger system sizes are needed to achive the same results as in the parallel ladder. This can not be stated for certain however and only further investigations into those models can clarify this issue.

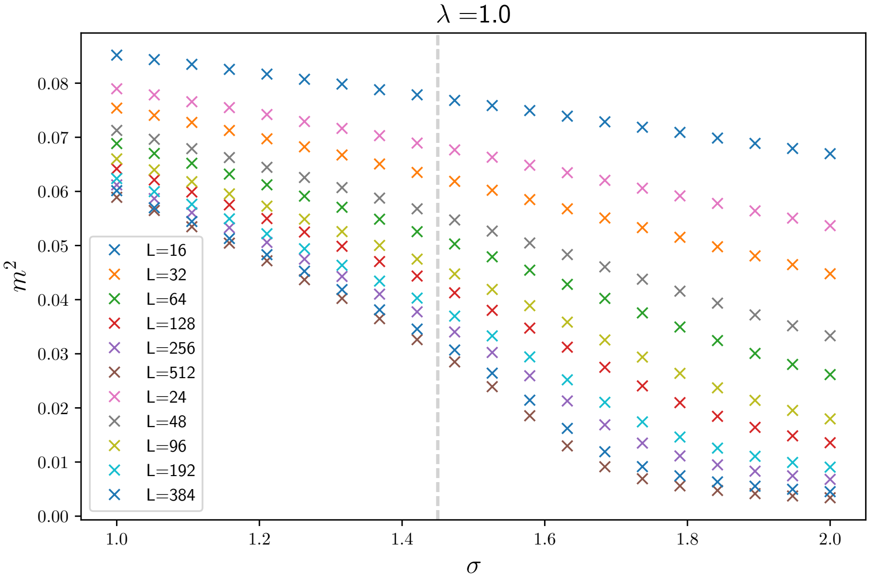

Figure 18: The squared staggered magnetization at $\lambda = 1$ on the $\mathcal{H}_\times$-ladder over varying σ (horizontal slice in the quantum phase diagram). The σ for which a problematic vertical slice in the quantum phase diagram is taken in Fig. 17b is marked with a dashed line.

6 Conclusion

In this thesis, two antiferromagnetic long-range Heisenberg spin-$\frac{1}{2}$ ladders were introduced and their phases and expected behavior were characterized. For the study of their quantum criticality the quantum Monte Carlo method of stochastic series expansion was applied. The implementation of states and updates in the SSE method together with the observables staggered magnetization and susceptibility was discussed. To investigate the critical behavior of the systems in the thermodynamic limit at zero temperature, systems of finite size at finite temperature were sampled in the quantum Monte Carlo method. Here, systems of a size up to 512 ladder rungs, corresponding to 1024 spins were simulated. The quantities of interest were the quantum critical point (σ_c, λ_c) together with the critical exponents ν, β and γ. To extract those, a cooling scheme for the simulation together with finite size methods were introduced. These were the utilization of Binder cumulants to extract the critical point as well as the so called "data collapse", which allowed the extraction of the critical points and exponents at once.

Equipped with these methods, the full quantum phase diagrams of the two ladder models were mapped out. The critical points derived here are in good agreement with previos works on these long-range models [1, 42] and qualitativly correspond to the theoretical approximation of linar spin waves.

It was confirmed, that there exists an upper critical σ, above which no long-range order exists and its value was estimated for both ladders. For the parallel long-range ladder model, the upper critical σ could be compared to results of the antiferromagnetic spin-$\frac{1}{2}$ long-range Heisenberg chain [25]. The critical σ of the chain and the ladder are not in good agreement here, the $\lambda \to \infty$-limit was clearly not reached by our simulations. For a better approximation to this limit, even larger systems have to be considered. It is a remaining problem for future investigations to confirm the correspondence of the parallel ladder model in the $\lambda \to \infty$ limit and the chain.

The results for the critical exponents were in good agreement with the long-range mean field theory below the upper critical dimension. Above the upper critical dimension, the results from this thesis expanded on results for these systems using the pCUT method. Where the critical exponents from that previous work [1] did not give satisfying physical behavior for large σ, the results here are much more well behaved and are in good agreement with theoretical predictions using functional renormalization group (FRG) methods [6]. There the qualitative behavior at large σ from FRG matches well with the critical exponents found here and the quantitative correspondence is also good.

One of the big take aways from this thesis is the novelty of the data produced here. It is an achievement, that the results for the aforementioned long-range ladder models obtained by QMC methods for large systems (up to 1024 spins) and the whole phase diagram were not only successfully extracted but are also in good agreement wit previos works and in certain aspects expand on them.

The issues in this work were primarily the extraction of data at higher σ, especially in the domain in the phase diagram, where the phase transition gets steep. There is no rigorous way (like the data collapse) to exctract the critical exponents in this region, where data at constant λ is considered. In particular, the extraction of the critical exponent ν is possible, but difficult in this region, further work could clarify the results there. Another future point of interest could be the aforementioned transition from the parallel ladder model to the spin-$\frac{1}{2}$ chain. Here, no smooth transition from one to the other could be found because of simulation limitations, although such a similarity is expected.

References

[1] Patrick Adelhardt and Kai P. Schmidt. Continuously varying critical exponents in long-range quantum spin ladders. *SciPost Physics*, 15(3):087, 2023.

[2] Matthias Bartelmann, Björn Feuerbacher, Timm Krüger, Dieter Lüst, Anton Rebhan, and Andreas Wipf. *Theoretische Physik 4— Thermodynamik und Statistische Physik*. Springer, 2018.

[3] Hans Bethe. Zur theorie der metalle: I. eigenwerte und eigenfunktionen der linearen atomkette. *Zeitschrift für Physik*, 71(3):205–226, 1931.

[4] Kurt Binder and Dieter W. Heermann. *Monte Carlo simulation in statistical physics: an introduction*. Springer, 4th, ed. edition, 2002.

[5] Elbio Dagotto and TM Rice. Surprises on the way from one-to two-dimensional quantum magnets: The ladder materials. *Science*, 271(5249):618–623, 1996.

[6] Nicolò Defenu, Alessandro Codello, Stefano Ruffo, and Andrea Trombettoni. Criticality of spin systems with weak long-range interactions. *Journal of Physics A: Mathematical and Theoretical*, 53(14):143001, 2020.

[7] Nicolò Defenu, Tobias Donner, Tommaso Macrì, Guido Pagano, Stefano Ruffo, and Andrea Trombettoni. Long-range interacting quantum systems. *Reviews of Modern Physics*, 95(3):035002, 2023.

[8] W Dieterich. Theorie der phasenübergänge. Technical report, Universität Konstanz, 2000.

[9] Amit Dutta and JK Bhattacharjee. Phase transitions in the quantum ising and rotor models with a long-range interaction. *Physical Review B*, 64(18):184106, 2001.

[10] Cardy J. (ed.). *Finite-Size Scaling*. Elsevier, 1988.

[11] Sebastian Fey, Sebastian C Kapfer, and Kai Phillip Schmidt. Quantum criticality of two-dimensional quantum magnets with long-range interactions. *Physical review letters*, 122(1):017203, 2019.

[12] Sebastian Fey and Kai Phillip Schmidt. Critical behavior of quantum magnets with long-range interactions in the thermodynamic limit. *Physical Review B*, 94(7):075156, 2016.

[13] Michael E. Fisher and Michael N. Barber. Scaling theory for finite-size effects in the critical region. *Phys. Rev. Lett.*, 28:1516–1519, Jun 1972.

[14] Jeffrey Goldstone. Field theories with ≪superconductor≫ solutions. *Il Nuovo Cimento (1955-1965)*, 19:154–164, 1961.

[15] Jeffrey Goldstone, Abdus Salam, and Steven Weinberg. Broken symmetries. *Physical Review*, 127(3):965, 1962.

[16] Sudha Gopalan, TM Rice, and M Sigrist. Spin ladders with spin gaps: A description of a class of cuprates. *Physical Review B*, 49(13):8901, 1994.

[17] Bertrand I Halperin. On the hohenberg-mermin-wagner theorem and its limitations. *Journal of Statistical Physics*, 175(3):521–529, 2019.

[18] Pierre C Hohenberg. Existence of long-range order in one and two dimensions. *Physical Review*, 158(2):383, 1967.

[19] Theodore Holstein and Henry Primakoff. Field dependence of the intrinsic domain magnetization of a ferromagnet. *Physical Review*, 58(12):1098, 1940.

[20] TR Kirkpatrick and D Belitz. Exponent relations at quantum phase transitions with applications to metallic quantum ferromagnets. *Physical Review B*, 91(21):214407, 2015.

[21] Jan Koziol, Sebastian Fey, Sebastian C Kapfer, and Kai Phillip Schmidt. Quantum criticality of the transverse-field ising model with long-range interactions on triangular-lattice cylinders. *Physical Review B*, 100(14):144411, 2019.

[22] Jan Alexander Koziol, Anja Langheld, Sebastian C Kapfer, and Kai Phillip Schmidt. Quantum-critical properties of the long-range transverse-field ising model from quantum monte carlo simulations. *Physical Review B*, 103(24):245135, 2021.

[23] W. Krauth. *Statistical Mechanics: Algorithms and Computations*. Oxford Master Series in Physics. Oxford University Press, UK, 2006.

[24] Thaddeus D Ladd, Fedor Jelezko, Raymond Laflamme, Yasunobu Nakamura, Christopher Monroe, and Jeremy Lloyd O'Brien. Quantum computers. *nature*, 464(7285):45–53, 2010.

[25] Nicolas Laflorencie, Ian Affleck, and Mona Berciu. Critical phenomena and quantum phase transition in long range heisenberg antiferromagnetic chains. *Journal of Statistical Mechanics: Theory and Experiment*, 2005(12):P12001, 2005.

[26] Bella Lake, D Alan Tennant, Chris D Frost, and Stephen E Nagler. Quantum criticality and universal scaling of a quantum antiferromagnet. *Nature materials*, 4(4):329–334, 2005.

[27] Anja Langheld. Quantum-critical properties of the one-dimensional long-range transverse-field ising model extracted by quantum monte carlo simulations. 2021.

[28] Anja Langheld, Jan Alexander Koziol, Patrick Adelhardt, Sebastian Kapfer, and Kai P. Schmidt. Scaling at quantum phase transitions above the upper critical dimension. *SciPost Physics*, 13(4):088, 2022.

[29] EY Loh Jr, JE Gubernatis, RT Scalettar, SR White, DJ Scalapino, and RL Sugar. Sign problem in the numerical simulation of many-electron systems. *Physical Review B*, 41(13):9301, 1990.

[30] N David Mermin and Herbert Wagner. Absence of ferromagnetism or antiferromagnetism in one-or two-dimensional isotropic heisenberg models. *Physical Review Letters*, 17(22):1133, 1966.

[31] Christopher Monroe, Wes C Campbell, L-M Duan, Z-X Gong, Alexey V Gorshkov, Paul W Hess, Rajibul Islam, Kihwan Kim, Norbert M Linke, Guido Pagano, et al. Programmable quantum simulations of spin systems with trapped ions. *Reviews of Modern Physics*, 93(2):025001, 2021.

[32] Yoichiro Nambu. Quasi-particles and gauge invariance in the theory of superconductivity. *Physical Review*, 117(3):648, 1960.

[33] Lev Pitaevskii and Sandro Stringari. Uncertainty principle, quantum fluctuations, and broken symmetries. *Journal of low temperature physics*, 85:377–388, 1991.

[34] Sachdev S. *Quantum Phase Transitions.* Cambridge University Press, 2ed. edition, 2011.

[35] Anders W. Sandvik. A generalization of handscomb's quantum monte carlo scheme-application to the 1d hubbard model. *Journal of Physics A: Mathematical and General*, 25(13):3667, Jul 1992.

[36] Anders W. Sandvik. Finite-size scaling of the ground-state parameters of the two-dimensional heisenberg model. *Phys. Rev. B*, 56:11678–11690, Nov 1997.

[37] Anders W. Sandvik. Computational Studies of Quantum Spin Systems. *AIP Conference Proceedings*, 1297(1):135–338, 11 2010.

[38] Kai P Schmidt and Götz S Uhrig. Excitations in one-dimensional s= 1 2 quantum antiferromagnets. *Physical review letters*, 90(22):227204, 2003.

[39] Olav F. Syljuåsen and Anders W. Sandvik. Quantum monte carlo with directed loops. *Phys. Rev. E*, 66:046701, Oct 2002.

[40] Simon Trebst, Hartmut Monien, Chris J Hamer, Zheng Weihong, and Rajiv RP Singh. Strong-coupling expansions for multiparticle excitations: continuum and bound states. *Physical Review Letters*, 85(20):4373, 2000.

[41] Matthias Troyer and Uwe-Jens Wiese. Computational complexity and fundamental limitations to fermionic quantum monte carlo simulations. *Phys. Rev. Lett.*, 94:170201, May 2005.

[42] Luhang Yang, Phillip Weinberg, and Adrian E. Feiguin. Topological to magnetically ordered quantum phase transition in antiferromagnetic spin ladders with long-range interactions. *SciPost Phys.*, 13:060, 2022.

[43] Eddy Yusuf, Anuvrat Joshi, and Kun Yang. Spin waves in antiferromagnetic spin chains with long-range interactions. *Physical Review B*, 69(14):144412, 2004.

Acknowledgments

I am grateful for the support of my supervisor Prof. Dr. Kai Phillip Schmidt, who always had an open ear for my questions during my research on this thesis and with whom I was in constant contact regarding the contents and structure of the research and the final thesis.

I would also like to thank my colleague Patrick Adelardt, who was always available to answer questions on the models and physical topics. As well as my colleagues Jan Koziol, Anja Langheld and Calvin Krämer, who introduced me to the SSE QMC method and to whom I could always turn when I had questions of a physical or technical nature.

Eigenständigkeitserklärung

Hiermit versichere ich, dass ich die vorliegende Masterarbeit selbstständig verfasst habe. Ich versichere, dass ich keine anderen als die angegebenen Quellen benutzt und alle wörtlich oder sinngemäß aus anderen Werken übernommenen Aussagen als solche kenntlich gemacht habe. Des Weiteren versichere ich, dass diese Arbeit weder vollständig noch in wesentlichen Teilen Gegenstand eines anderen Prüfungsverfahren gewesen ist.

Erlangen, den 24. Mai 2024

Florian Simon